

## Synthesis, Structure, and Zero-Field SMM Behavior of Homometallic Dy<sub>2</sub>, Dy<sub>4</sub>, and Dy<sub>6</sub> Complexes

Pawan Kumar, Abinash Swain, Joydev Acharya, Yanling Li, Vierandra Kumar, Gopalan Rajaraman,\* Enrique Colacio,\* and Vadapalli Chandrasekhar\*



Cite This: *Inorg. Chem.* 2022, 61, 11600–11621



Read Online

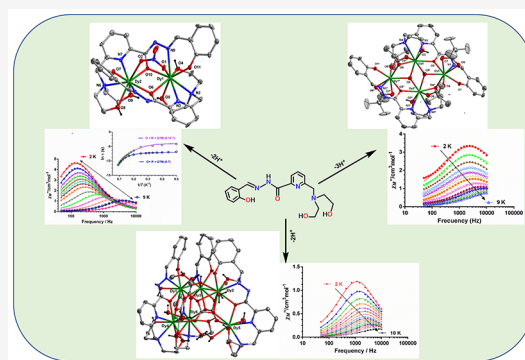
ACCESS |

Metrics & More

Article Recommendations

Supporting Information

**ABSTRACT:** The synthesis, structure, and magnetic properties of three Dy<sup>III</sup> complexes of different nuclearity, [Dy<sub>2</sub>(H<sub>2</sub>L)<sub>2</sub>(NO<sub>3</sub>)] [NO<sub>3</sub>]<sub>2</sub>·2H<sub>2</sub>O·CH<sub>3</sub>OH (1), [Dy<sub>4</sub>(HL)<sub>2</sub>(piv)<sub>4</sub>(OH)<sub>2</sub>] (2), and [Dy<sub>6</sub>(H<sub>2</sub>L)<sub>3</sub>(μ<sub>3</sub>-OH)(μ<sub>3</sub>-CO<sub>3</sub>)<sub>3</sub>(CH<sub>3</sub>OH)<sub>4</sub>(H<sub>2</sub>O)<sub>8</sub>] 5Cl·3H<sub>2</sub>O (3) [(H<sub>4</sub>L) = 6-((bis(2-hydroxyethyl)-amino)-N'-(2-hydroxybenzylidene)picolinohydrazide)], are described. This variety of complexes with the same ligand could be obtained by playing with the metal-to-ligand molar ratio, the type of Dy<sup>III</sup> salt, the kind of base, and the presence/absence of coligand. 1 is a dinuclear complex, while 2 is a tetranuclear assembly with a butterfly-shaped topology. 3 is a homometallic hexanuclear complex that exhibits a propeller-shaped topology. Interestingly, in this complex 3, three atmospheric carbon dioxide molecules are trapped in the form of carbonate ions, which assist in holding the hexanuclear complex together. All of the complexes reveal a slow relaxation of magnetization even in zero applied field. Complex 1 is a zero-field SMM with an effective energy barrier ( $U_{\text{eff}}$ ) of magnetization reversal equal to 87(1) K and a relaxation time of  $\tau_0 = 6.4(3) \times 10^{-9}$  s. Under an applied magnetic field of 0.1 T, these parameters change to  $U_{\text{eff}} = 101(3)$  K,  $\tau_0 = 2.5(1) \times 10^{-9}$  s. Complex 2 shows zero-field SMM behavior with  $U_{\text{eff}} = 31(2)$  K,  $\tau_0 = 4.2(1) \times 10^{-7}$  s or  $\tau_{01} = 2(1) \times 10^{-7}$  s,  $U_{\text{eff}2} = 37(8)$  K,  $\tau_{02} = 5(6) \times 10^{-5}$  s, and  $U_{\text{eff}2} = 8(4)$  K by considering two Orbach relaxation processes, while 3, also a zero-field SMM, shows a double relaxation of magnetization [ $U_{\text{eff}1} = 62.4(3)$  K,  $\tau_{01} = 4.6(3) \times 10^{-8}$  s, and  $U_{\text{eff}1} = 2(1)$  K,  $\tau_{02} = 4.6(2) \times 10^{-5}$  s]. The *ab initio* calculations indicated that in these complexes, the Kramer's ground doublet is characterized by an axial g-tensor with the prevalence of the  $m_j = \pm 15/2$  component, as well as that due to the weak magnetic coupling between the metal centers, the magnetic relaxation, which is dominated by the single Dy<sup>III</sup> centers rather than by the exchange-coupled states, takes place via Raman/Orbach or TA-QTM. Moreover, theoretical calculations support a toroidal magnetic state for complex 2.



### INTRODUCTION

There is considerable recent interest in the utility of appropriate lanthanide metal complexes as single-molecule magnets (SMMs) and single-ion magnets (SIMs).<sup>1–9</sup> This field got its breakthrough by the seminal discovery of Ishikawa and co-workers that the terbium phthalocyanine sandwich complex [Bu<sub>4</sub>N][TbPc<sub>2</sub>] is a single-molecule magnet with slow relaxation of magnetization.<sup>1</sup> This discovery prompted researchers to examine the favorable properties of lanthanide ions including a large unquenched spin–orbit coupling, which can result in substantial single-ion anisotropy.<sup>2</sup> In addition, many lanthanide ions have a reasonable ground-state spin owing to the presence of a large number of unpaired electrons. Finally, ions such as Dy<sup>III</sup> are Kramers ions with a bistable ground state. Because of this, a large number of Dy<sup>III</sup> complexes have been examined and found to be single-molecule magnets.<sup>3</sup> This area got a further boost by the discovery that the organometallic sandwich complexes, [Dy(Cp<sup>III</sup>)<sub>2</sub>][B(C<sub>6</sub>F<sub>5</sub>)<sub>4</sub>], where Cp<sup>III</sup> = (C<sub>5</sub>H<sub>2</sub><sup>1</sup>Bu<sub>3-1,2,4</sub>), and [(Cp<sup>iPr5</sup>)Dy(Cp\*)]<sup>+</sup> (Cp<sup>iPr5</sup>, penta-iso-propylcyclopentadienyl;

Cp\*, pentamethylcyclopentadienyl), show the highest blocking temperatures, temperatures below which the magnetization of the complexes is retained or blocked indefinitely.<sup>4</sup> These and other such organometallic complexes, while possessing extremely interesting magnetic properties are, however, extremely air- and moisture-sensitive, rendering their handling difficult. Air-stable complexes are therefore of interest, and there have been some examples of mononuclear complexes with good properties.<sup>5</sup> We have also been involved in such endeavors and have been to assemble mononuclear complexes in pentagonal bipyramidal and other geometries.<sup>6</sup>

In addition to mononuclear complexes, complexes with larger nuclearity have also been of interest because of a variety

Received: March 29, 2022

Published: July 18, 2022

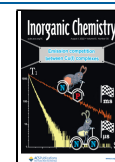


Table 1. Crystal Data and Structure Refinement Parameters of 1–3

complex	1	2	3
formula	C <sub>37</sub> H <sub>48</sub> Dy <sub>2</sub> N <sub>10</sub> O <sub>17</sub>	C <sub>56</sub> H <sub>76</sub> Dy <sub>4</sub> N <sub>8</sub> O <sub>18</sub>	C <sub>61</sub> H <sub>99</sub> N <sub>12</sub> O <sub>37</sub> Dy <sub>6</sub> Cl <sub>5</sub>
g/mol	1229.85	1799.24	2744.77
crystal system	trigonal	monoclinic	monoclinic
space group	R3c	P2 <sub>1</sub> /n	P2 <sub>1</sub> /n
a/Å	27.990(4)	12.129(5)	20.341(3)
b/Å	27.990(4)	16.468(5)	30.464(3)
c/Å	28.498(4)	17.663(5)	20.356(3)
α (deg)	90	90	90
β (deg)	90	94.941(2)	112.736(2)
γ (deg)	120	90	90
V/Å <sup>3</sup>	19 335(5)	3515(2)	11 634.0(3)
Z	18	2	4
ρ <sub>c</sub> /g cm <sup>-3</sup>	1.901	1.700	1.567
μ/mm <sup>-1</sup>	3.538	4.269	3.988
F(000)	10944.0	1752.0	5304.0
crystal size (mm <sup>3</sup> )	0.11 × 0.09 × 0.06	0.14 × 0.11 × 0.07	0.24 × 0.21 × 0.17
2θ range (deg)	5.042 to 56.598	8.154 to 50.052	8.18 to 52.044
limiting indices	−37 ≤ h ≤ 37 −37 ≤ k ≤ 37 −37 ≤ l ≤ 38	−14 ≤ h ≤ 13 −19 ≤ k ≤ 19 −21 ≤ l ≤ 20	−25 ≤ h ≤ 25 −37 ≤ k ≤ 37 −25 ≤ l ≤ 24
reflns collected	95 658	26 532	182 119
ind reflns	10 681 [R(int) = 0.0716]	6187 [R(int) = 0.0724]	22 821 [R(int) = 0.0349]
completeness to θ (%)	100	100	100
refinement method	full-matrix least squares on F <sup>2</sup>	full-matrix least squares on F <sup>2</sup>	full-matrix least squares on F <sup>2</sup>
data/restraints/params	10681/13/615	6187/3/383	22821/87/1175
goodness of fit on F <sup>2</sup>	1.034	1.033	1.026
final R indices [I > 2θ(I)]	R <sub>1</sub> = 0.0302 wR <sub>2</sub> = 0.0632	R <sub>1</sub> = 0.0491 wR <sub>2</sub> = 0.1066	R <sub>1</sub> = 0.0204 wR <sub>2</sub> = 0.0486
R indices (all data)	R <sub>1</sub> = 0.0424 wR <sub>2</sub> = 0.0674	R <sub>1</sub> = 0.0781 wR <sub>2</sub> = 0.1158	R <sub>1</sub> = 0.0220 wR <sub>2</sub> = 0.0491
CCDC no.	2162479	2162480	2162481

of reasons. Dinuclear complexes offer an opportunity to study the magnetic interactions between the two lanthanide centers.<sup>7</sup> Larger nuclearity complexes, particularly those containing Gd<sup>III</sup>, have attracted interest because of the possibility of harnessing the magnetocaloric effect.<sup>8</sup> Large anisotropic lanthanide ions such as Dy<sup>III</sup>, Tb<sup>III</sup>, and Ho<sup>III</sup> in multinuclear triangular, square, or hexagonal forms can result in toroidal and mixed toroidal systems, which depend strongly on the nuclearity and structural topology.<sup>9a–c</sup> Finally, it has also been of interest to understand the design of ligands, which allows a modulation of the nuclearity of the complexes as well as the coordination number and structural topology. Toward this end, we have been interested to probe whether a given ligand, under a small variation of reaction conditions including using co-ligands or stoichiometry or by varying the amount of base, can be used to assemble the complexes with varying nuclearity.

In this regard, the aroylhydrazone-based Schiff base ligands are quite remarkable. These ligands have suitable flexible coordination pockets involving C–C/C–N/N–N bond rotations, which allow a flexible coordination response. In addition, these ligands also have the flexibility of binding to the metal ions either in their keto form or in the enol form depending upon the reaction conditions.<sup>10</sup>

Because of these interesting features, we have been working with this family of ligands for some time with considerable success.<sup>10</sup> Recently, we have used one member of this family to

assemble a dinuclear Dy<sup>III</sup> complex, where the two Dy<sup>III</sup> are nonequivalent.<sup>10e</sup>

Motivated by the above result, we were interested in the possibility of using this ligand, H<sub>4</sub>L, [(H<sub>4</sub>L) = 6-((bis(2-hydroxyethyl)amino)-N'-(2-hydroxybenzylidene)-picolinohydrazide)] and examine if the *same* ligand under different reaction conditions can allow the assembly of complexes with varying nuclearity. This is a concept that we have explored earlier<sup>10c</sup> and were interested to see its implementation with H<sub>4</sub>L. Accordingly, herein, we report the synthesis, structural characterization, and magnetic studies of [Dy<sub>2</sub>(H<sub>2</sub>L)<sub>2</sub>(NO<sub>3</sub>)<sub>2</sub>]·NO<sub>3</sub>·2H<sub>2</sub>O·CH<sub>3</sub>OH (1), [Dy<sub>4</sub>(HL)<sub>2</sub>(piv)<sub>4</sub>(OH)<sub>2</sub>] (2), and [Dy<sub>6</sub>(H<sub>2</sub>L)<sub>3</sub>(μ<sub>3</sub>-OH)(μ<sub>3</sub>-CO<sub>3</sub>)<sub>3</sub>(CH<sub>3</sub>OH)<sub>4</sub>(H<sub>2</sub>O)<sub>8</sub>]·5Cl<sub>2</sub>·3H<sub>2</sub>O (3). Detailed magnetic studies reveal that 1–3 are zero-field SMMs. Moreover, the origin of magnetic relaxation and the role of magnetic exchange have been studied in detail by theory, which also allowed establishing the toroidal magnetic state for complex 2.

## EXPERIMENTAL SECTION

Solvents and other general reagents used in this work were purified according to standard procedures.<sup>11</sup> Pyridine-2,6-dicarboxylic acid, sodium borohydride, pivalic acid, tetrabutylammonium hydroxide solution (40 wt % in water), DyCl<sub>3</sub>·6H<sub>2</sub>O, and Dy(NO<sub>3</sub>)<sub>3</sub>·5H<sub>2</sub>O were obtained from Sigma-Aldrich Chemical Co. and were used as received. Hydrazine hydrate (80%), diethanolamine, PBr<sub>3</sub>, and sodium sulfate (anhydrous) were obtained from SD Fine Chemicals, Mumbai, India.

**Instrumentation.** Melting points were measured using a JSGW melting point apparatus and are uncorrected. IR spectra were recorded as KBr pellets on a Bruker Vector 22 FT IR spectrophotometer operating between 400 and 4000  $\text{cm}^{-1}$ . Elemental analyses of the compounds were obtained using Thermoquest CE Instruments CHNS-O, E.A./110 model. Electrospray ionization mass spectra (ESI-MS) were recorded on a MICROMASS QUATPRO II triple quadrupole mass spectrometer.  $^1\text{H}$  NMR spectra were recorded in  $\text{CDCl}_3$  and  $\text{DMSO}-d_6$  solutions on a JEOL JNM LAMBDA 400 model spectrometer operating at 500.0 MHz, Chemical shifts are reported in parts per million (ppm) and are referenced with respect to internal tetramethyl silane ( $^1\text{H}$ ).

**X-ray Crystallography.** Single-crystal data for **1** and **2** were collected on a Bruker SMART CCD diffractometer (Mo  $K\alpha$  radiation,  $\lambda = 0.71073$  Å) at 100 K. The program SMART<sup>12a</sup> was used for collecting frames of data, indexing reflections, and determining lattice parameters, SAINT<sup>12a</sup> for integration of the intensity of reflections and scaling, SADABS<sup>12b</sup> for absorption correction, and SHELXTL<sup>12c</sup> for space group and structure determination and least-squares refinements on  $F^2$ . X-ray diffraction data for complex **3** were collected at 120 K using a Rigaku diffractometer with graphite-monochromated molybdenum  $K\alpha$  radiation,  $\lambda = 0.71073$  Å. Data integration and reduction were processed with CrysAlisPro software.<sup>12d</sup> An empirical absorption correction was applied to the collected reflections with SCALE3 ABSPACK integrated with CrysAlisPro. The crystal structures were solved and refined by full-matrix least-squares methods against  $F^2$  using the program SHELXL-2014<sup>12e</sup> using Olex2<sup>12f</sup> software. All of the nonhydrogen atoms were refined with anisotropic displacement parameters. Hydrogen positions were fixed at calculated positions and refined isotropically. The crystallographic figures were generated using Diamond 3.1e software.<sup>12g</sup> In addition, some disordered solvent molecules were present in complexes **2** and **3**. We could not assign all of the solvent molecules properly due to the disorder and weak residual Q peaks. So, the Olex-2 mask program was performed to discard the disordered solvent molecules. The possible masked electron counts and void volumes have been included in the corresponding crystallographic information files (CIFs).

The crystal data, the cell parameters, and CCDC information for all of the complexes are given in Table 1.

**Magnetic Properties.** Static (dc) and dynamic (ac) magnetic susceptibility measurements were carried out using, respectively, a Quantum Design MPMS-XL-7 SQUID magnetometer and a PPMS-9 (ACMS option) on polycrystalline powder samples. The dc measurements were performed in the temperature range of 2–300 K under a magnetic field of 0.5 T (20–300 K) and 0.05 T (40–2 K), whereas the ac measurements were carried out in the temperature range of 2.5–15 K under an oscillating field of 10 Oe within the frequency range of 50–279 Hz and of 3 Oe within the frequency range of 354–10000 Hz, under static fields of 0 and 2000 Oe. The magnetic susceptibility values were corrected from the diamagnetism of the molecular constituents and of the sample holder. The sample (about 15 mg) wrapped in a piece of parafilm (about 25 mg) and packed in a polyethylene bag was pelletized to avoid reorientation at low temperature and high field. It was introduced in the SQUID at 200 K under helium flow and frozen before purging under vacuum.

**Computational Details.** All of the calculations were performed using the MOLCAS 8.2<sup>13a</sup> suit program using CASSCF/RASSI-SO/SINGLE\_ANISO/POLY\_ANISO module on the X-ray obtained crystal structures without further modeling.<sup>13b–g</sup> A TZVP quality of basis set has been used for the metal ion, for the surrounding coordinating atom, a DZV level, and for the rest of the atoms, SVP level of basis set has been used from the ANO-RCC library.<sup>13h,i</sup> The relativistic effect has been taken into consideration using the DKH Hamiltonian.<sup>13j</sup> Cholesky decomposition was utilized to save storage space generated by one integral. Active space of nine electrons in 7f orbitals was taken for all calculations with 21 roots in the RASSI-SO step.<sup>13k</sup> First, single-ion anisotropy calculations have been performed on the individual  $\text{Dy}^{\text{III}}$  centers by replacing the other  $\text{Dy}^{\text{III}}$  ion with the  $\text{Lu}^{\text{III}}$  ions. The calculations were carried out on the entire complex without further modeling to attain the most reliable values. This gives

the magnetic properties offered by the individual  $\text{Dy}^{\text{III}}$  centers. The single aniso input taken from the single aniso calculations has been used in the POLY\_ANISO module to gain insight into the overall magnetic properties of the complexes originating from the exchanged coupled states. The fitted exchange parameters were further verified by density functional calculations using Gaussian 16<sup>13l</sup> package with the hybrid B3LYP/CSDZ/TZV methods by replacing the  $\text{Dy}^{\text{III}}$  with  $\text{Gd}^{\text{III}}$  and then rescaling it by multiplying with a factor of 5/7.<sup>13m–o,10e</sup> For complex **2**, the  $dM/dH$  vs  $H$  plot seems to indicate the presence of an S-shape plot for the  $M$  vs  $H$  plot at a very low field (see the Supporting Information (SI)). This behavior points out the possibility of a mixed toroidal moment for the above complex. Hence, using the POLY\_ANISO module, the toroidal behavior for complex **2** has been investigated.<sup>13p</sup>

**Synthesis.** The ligand  $\text{H}_4\text{L}$  was prepared according to the procedure we reported recently.<sup>10e</sup>

**Synthesis of 1–3.**  $[\text{Dy}_2(\text{H}_2\text{L})_2(\text{NO}_3)] [\text{NO}_3] \cdot 2\text{H}_2\text{O} \cdot \text{CH}_3\text{OH}$  (**1**).  $\text{Dy}(\text{NO}_3)_3 \cdot 5\text{H}_2\text{O}$  (0.048 g, 0.11 mmol) was added to a methanol solution (30 mL) of  $\text{H}_4\text{L}$  (0.040 g, 0.11 mmol) at room temperature affording a yellow colored solution. Then, triethylamine (0.046 mL, 0.33 mmol) was added, and the reaction mixture was stirred overnight at room temperature. The resulting solution was then filtered, and the filtrate stripped off its solvent in vacuo affording a solid yellow residue, which was dissolved in methanol (5 mL) and kept for slow evaporation. Suitable X-ray quality crystals were formed within 3–4 days. Yield: 0.051 g, 76.1% (based on the  $\text{Dy}^{\text{III}}$  salt). Mp: >250 °C (d). IR (KBr)  $\text{cm}^{-1}$ : 3385 (br), 3205 (br), 2971 (br), 1611 (s), 1557 (w), 1537 (s), 1477 (s), 1453 (w), 1429, 1384 (s), 1261 (w), 1199 (s), 1143 (s), 1068 (s), 1004 (w), 880 (s), 850 (s), 800 (w), 760 (s), 713 (w), 690 (s), 598 (s), 534 (s). Anal. Calcd for  $\text{C}_{37}\text{H}_{48}\text{Dy}_2\text{N}_{10}\text{O}_{17}$  (1232.1782): C, 36.14; H, 3.93; N, 11.39. Found: C, 36.05; H, 3.72; N, 11.19.

$[\text{Dy}_4(\text{LH})_2(\text{piv})_4(\text{OH})_2]$  (**2**). Solid  $\text{DyCl}_3 \cdot 6\text{H}_2\text{O}$  (0.082 g, 0.22 mmol) and  $\text{H}_4\text{L}$  (0.040 g, 0.11 mmol) were taken in methanol (30 mL) and then stirred for 5 min at room temperature. Then, tetrabutylammonium hydroxide (0.55 mmol) was added to this mixture in a dropwise manner. After 15 min, pivalic acid (0.22 mmol) was added and the reaction mixture was stirred for 8 h at room temperature. All of the volatiles were removed from the reaction mixture in vacuo affording a semisolid yellow residue, which was dissolved in a mixture of methanol (5 mL) and chloroform (2 mL) and kept for crystallization by slow evaporation. Suitable crystals were harvested in 2–3 days.

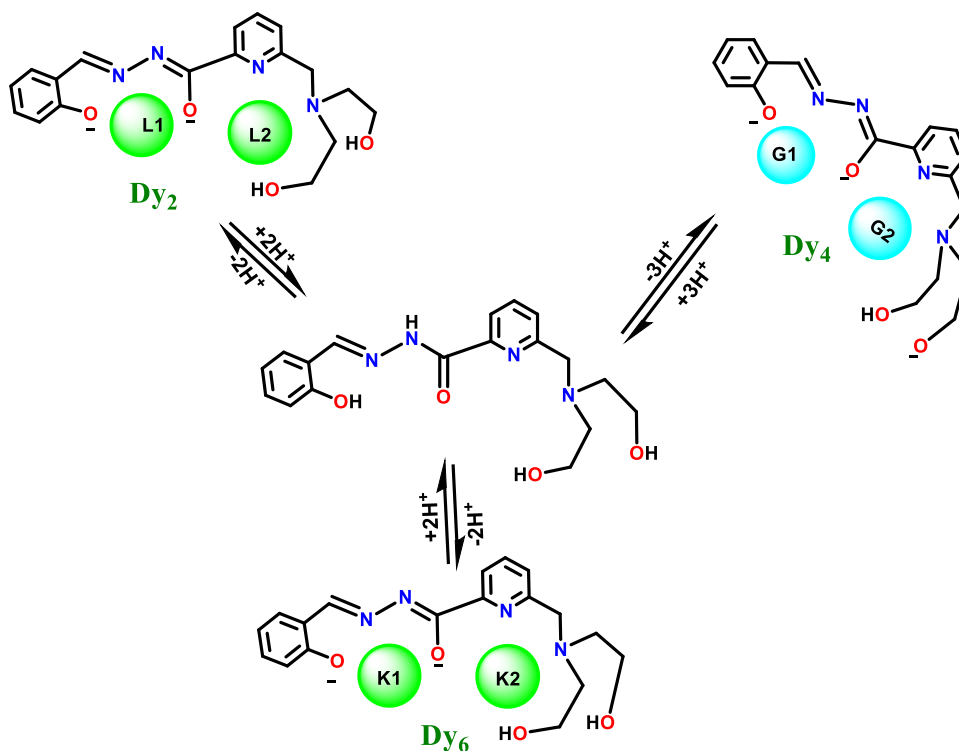
Yield: 0.047, 47.9%. IR (KBr)  $\text{cm}^{-1}$ : 3424 (br), 2959 (br), 2865 (br), 1612 (s), 1571 (w), 1556.33 (s), 1476 (s), 1425 (s), 1377 (s), 1350 (s), 1227 (s), 1195 (s), 1079 (s), 1014 (w), 901 (s), 848 (s), 756 (s), 656 (w), 595 (s). Anal. Calcd for  $\text{C}_{56}\text{H}_{76}\text{Dy}_4\text{N}_{10}\text{O}_{17}$  (1804.2444): C, 37.13; H, 4.23; N, 7.73. Found: C, 36.91; H, 4.05; N, 7.51.

$[\text{Dy}_6(\text{H}_2\text{L})_3(\mu_3-\text{OH})(\mu_3-\text{CO}_3)_3(\text{CH}_3\text{OH})_4(\text{H}_2\text{O})_8]$   $5\text{Cl} \cdot 3\text{H}_2\text{O}$  (**3**).  $\text{DyCl}_3 \cdot 6\text{H}_2\text{O}$  (0.082 g, 0.22 mmol) and  $\text{H}_4\text{L}$  (0.040 g, 0.11 mmol) were dissolved in methanol (30 mL) and then stirred vigorously for 10 min at room temperature. Then, triethylamine (0.33 mmol) was added slowly to the solution dropwise and the reaction mixture stirred for 7 h. After this, the volatiles in the reaction mixture were removed in vacuo to afford a solid yellow residue, which was dissolved in a mixture of methanol (5 mL) and chloroform (5 mL) and kept for crystallization by slow evaporation. Suitable crystals were obtained in 2–3 days. Yield: 0.045 g, 45.4% (based on the  $\text{Dy}^{\text{III}}$  salt). Mp: >200 °C (d). IR (KBr)  $\text{cm}^{-1}$ : 3375 (br), 1616 (s), 1560 (w), 1536 (w), 1476 (s), 1441 (w), 1351 (s), 1262 (w), 1201 (w), 1151 (s), 1123 (w), 1081 (s), 1016 (s), 916 (w), 892 (w), 796 (w), 691 (w), 520 (s). Anal. Calcd for  $\text{C}_{61}\text{H}_{99}\text{Dy}_6\text{N}_{12}\text{O}_{37}\text{Cl}_5$  (2750.0427): C, 26.69; H, 3.64; N, 6.12. Found: C 25.95; H, 4.15; N, 5.60.

## RESULTS AND DISCUSSION

**Synthetic Aspects.** As discussed above, the versatile coordination possibilities of the aroylhydrazone-based Schiff base ligands have been attracting our attention. We have utilized the ligand  $\text{H}_4\text{L}$  in the current investigations. This

**Scheme 1.** Unsymmetrical Coordination Pockets, Conformations Based on Base-Assisted Reversible Keto-Enol Tautomerization, and Coordination Modes of  $H_4L$  as Observed in Complexes 1–3



ligand has broadly two coordination pockets: a pentadentate (2N, 3O) and a tridentate (2O, 1N). In addition, the coordination can be influenced by the extent of deprotonation as well as the choice of keto vs enolate coordination. These features allowed us to assemble  $Dy_2$  (1),  $Dy_4$  (2), and  $Dy_6$  (3) complexes. In the case of  $Dy_2$  and  $Dy_6$  systems, the ligand binds to the metal center in its doubly deprotonated form  $[H_2L]^{2-}$ , while in  $Dy_4$  in its triply deprotonated form  $[HL]^{3-}$ . In the latter, one arm of diethanolamine is deprotonated. In all of the complexes, the ligand utilized the enolate oxygen to bridge two lanthanide centers (Scheme 1).

The reaction of  $H_4L$  and  $Dy(NO_3)_3 \cdot 5H_2O$  in the presence of  $Et_3N$  in a stoichiometric ratio of 1:1:2 in methanol at room temperature afforded a dinuclear complex  $[Dy_2(H_2L)_2(\mu_2-\eta^1:\eta^1-NO_3)] \cdot NO_3 \cdot 2MeOH \cdot H_2O$  (1) (Scheme 2). On the other hand, changing the metal-to-ligand ratio in the reaction of  $H_4L$  and  $DyCl_3 \cdot 6H_2O$  in the presence of  $Et_3N$  in methanol in a stoichiometric ratio of 1:2:2 afforded the hexanuclear complex,  $[Dy_6(H_2L)_3(\mu_3-OH)(\mu_3-CO_3)_3(CH_3OH)_4(H_2O)_8] \cdot 5Cl \cdot 3H_2O$  (3) (Scheme 2). Changing the base from triethylamine to tetrabutylammonium hydroxide in the reaction of  $H_4L$ ,  $DyCl_3 \cdot 6H_2O$  along with pivalic acid as a coligand in a stoichiometric ratio of 1:2:2:5 afforded the tetranuclear complex  $[Dy_4(HL)_2(\mu_3-OH)_2(Piv)_4]$  (2) (Scheme 2).

It is interesting to note that in the presence of the stronger base tetrabutylammonium hydroxide, in addition to deprotonation at the phenol and enol sites, one of the diethanolamine arms is also deprotonated. Along with a hydroxide ligand, the deprotonated diethanolamine oxygens serve to connect the lanthanide centers that are present in a defective cubane structure (Scheme 2). The formation of the hexanuclear cluster is accomplished by the involvement of carbonate ligands, which is the result of the activation of atmospheric  $CO_2$ . The formation of carbonate ligands in situ under such basic

reaction conditions is not new. Uptake of atmospheric  $CO_2$  as carbonate ligand has been reported for 3d, 3d-4f, and 4f complexes.<sup>14</sup> We have observed this in the formation of tetranuclear lanthanide complex a few years ago (Figure S1).<sup>14f</sup>

The various reported binding modes of carbonate ligand in the complexes are given in Figure 1.

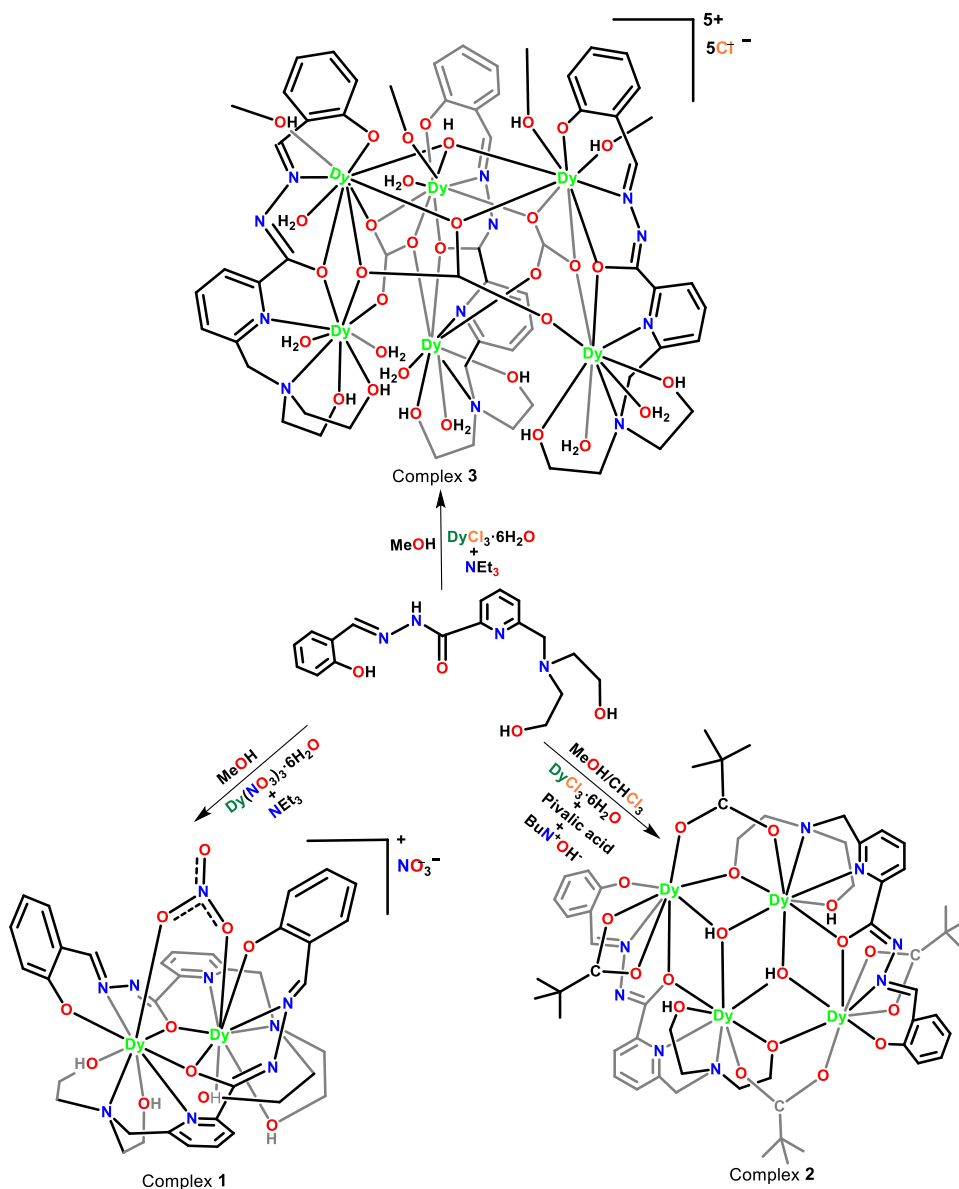
To ascertain that the atmospheric  $CO_2$  is indeed involved, we carried out the same reaction under completely inert conditions. We did not observe the formation of 3. Identification of carbonate ligand in complex 3 is done carefully by consideration of charge balance and single-crystal X-ray diffraction (SC-XRD) crystal data. Absorption bands in the IR spectrum for 3 found at 1441 and 839  $cm^{-1}$  can be assigned for carbonate ligand. These absorption bands are fully consistent with those observed for other carbonate complexes reported previously.<sup>14f,h,k</sup>

To check the phase purity of the complexes, powder X-ray diffraction measurement for complexes was done and found that the sequence and pattern of the peaks are in reasonable agreement with the simulated data obtained from single-crystal data (Figures S2–S4).

**X-ray Crystallography.** To elucidate the molecular structures of the complexes, we carried out single-crystal X-ray diffraction analysis. Complex 1 crystallized in the trigonal,  $R3c$  space group ( $Z = 18$ ). The asymmetric unit consists of the full monocationic dinuclear motif  $[Dy_2(H_2L)(\mu_2-NO_3)]^+$  along with a nitrate counter ion. A perspective view of 1 is given in Figure 2, and the selected bond parameters are provided in the caption of Figure 2.

The dinuclear assembly is built with the assistance of two doubly deprotonated  $H_2L^{2-}$  ligands. The two  $Dy^{III}$  centers are bound by the coordination pockets described above and are bridged by the enolate oxygen atom (Figure S5). One of the

## Scheme 2. Synthesis of 1–3



nitrate anions bridges the two Dy<sup>III</sup> centers, while the other remains as a counter anion. (Figure S5).

As can be seen from the above description, the formation of **1** involved the complete utilization of *all* of the coordination sites of (H<sub>2</sub>L<sup>2-</sup>). The central Dy<sub>2</sub>O<sub>2</sub> core is nonplanar with a dihedral angle of 109.96°(19) (Figure 3). The other metric parameters are given in the caption of Figure 2.

Both the Dy<sup>III</sup> centers in the complex are nine-coordinate (6O, 3N) in a spherical tricapped trigonal prism geometry as revealed by the SHAPE analysis program (Figure S6 and Table S1).<sup>15a,b</sup>

Among all of the bond distances, the shortest ones are those that involve the phenolate oxygen [Dy1–O11, 2.181(6) Å and Dy2–O7 = 2.189(6) Å].

Analysis of the crystal packing diagram of **1** reveals that the shortest distance between two Dy<sup>III</sup> centers of the neighboring molecule is 8.212 Å. (Figure S7), and the intrametallic distance between two Dy<sup>III</sup> centers of the molecule is 3.973(7) Å.

The crystal structure of **1** reveals the presence of intra- and intermolecular hydrogen bonds leading to the formation of a supramolecular structure (Figures S8–S9 and Tables S2–S3).

Complex **2** crystallized in the monoclinic, *P*<sub>2</sub><sub>1</sub>/*n* space group. The asymmetric unit [Dy<sub>2</sub>(LH)(μ<sub>2</sub>-η<sup>1</sup>η<sup>1</sup>Piv)(η<sup>2</sup>-Piv)(OH)] comprised half of the full molecule and consisted of one triply deprotonated HL<sup>3-</sup> ligand, which binds two Dy<sup>3+</sup> centers along with two pivalate ligands (Figure 4). The neutral tetranuclear assembly is composed of two defective cubes through edge and face sharing (Figure 4). The selected bond angles and bond lengths of the complex are provided in the caption of Figure 4.

The proliferation from the dinuclear motif to the tetranuclear complex occurs primarily as a result of the bridging coordination of the deprotonated diethanolamine arms. In addition, two μ<sub>3</sub>-OH ligands assist in binding three Dy<sup>III</sup> together. Among the pivalate ligands while one binds in a chelating anisobidentate manner with one Dy<sup>III</sup> [(Dy1–O6 = 2.555(8) Å, Dy1–O7 = 2.432(7) Å)], the other functions as a

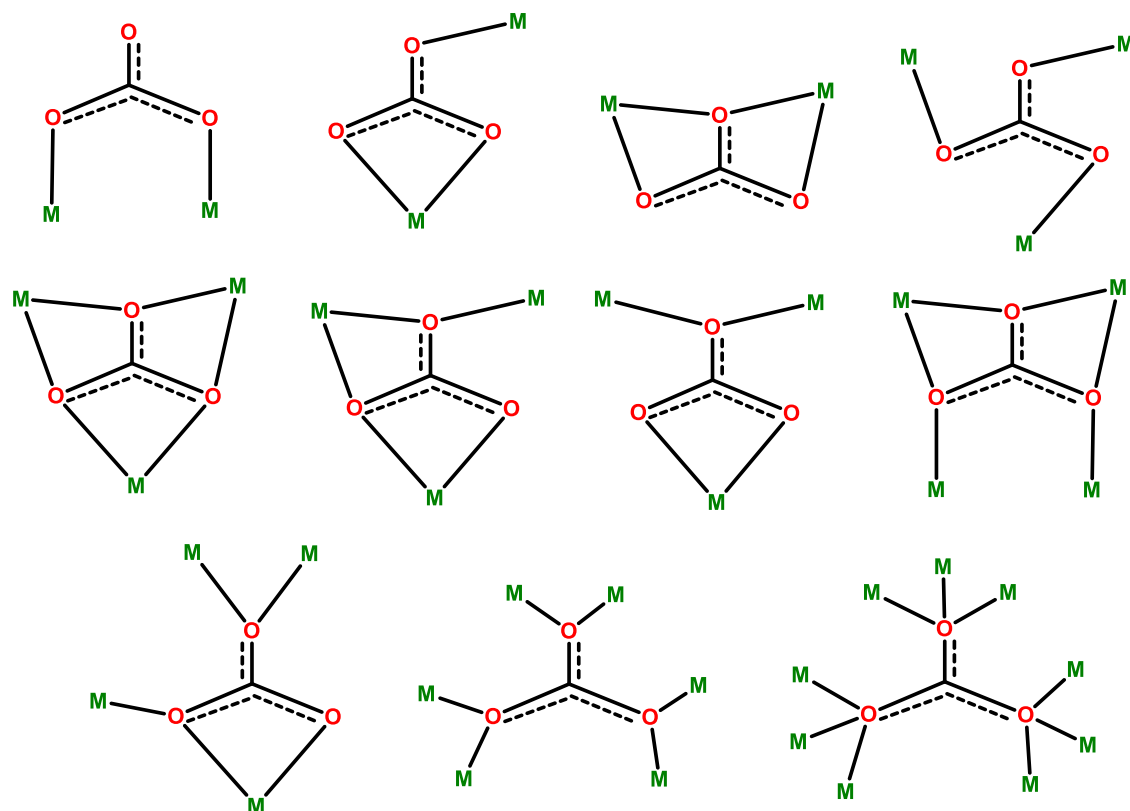


Figure 1. Some common binding modes of carbonate ligand in metal complexes.<sup>14</sup>

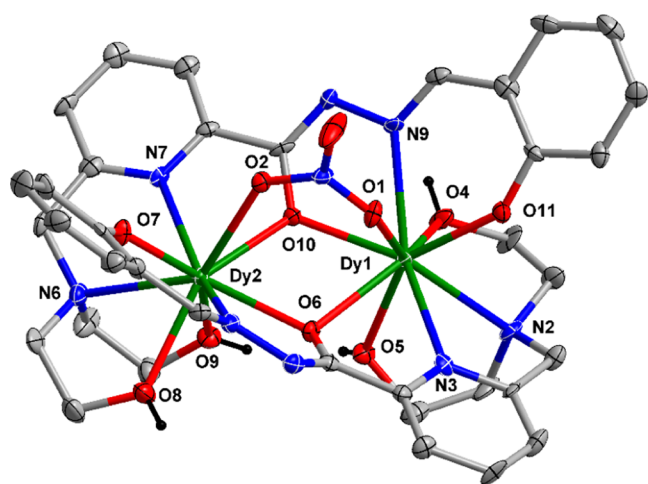


Figure 2. (a) Molecular structure of **1**. Thermal ellipsoids at a 50% probability level are shown (selected hydrogen atoms and the solvent molecules have been omitted for clarity). Color codes: N = blue; O = red; C = gray; Dy = dark green, and H = black. Selected bond lengths (Å) for **1**: for Dy1; Dy1–O1, Dy1–O4, Dy1–O5, Dy1–O6, Dy1–O10, Dy1–O11, Dy1–N2, Dy1–N3, and Dy1–N9 are 2.469(6), 2.419(6), 2.483(6), 2.497(6), 2.325(6), 2.181(6), 2.624(7), 2.506(11), and 2.513(7), respectively, for Dy2; Dy2–O2, Dy2–O6, Dy2–O7, Dy2–O8, Dy2–O9, Dy2–O10, Dy2–N5, Dy2–N6, and Dy2–N7 are 2.457(6), 2.324(6), 2.189(6), 2.448(7), 2.446(6), 2.510(6), 2.578(7), and 2.531(10) respectively, and selected bond angles for **1**: Dy1–O10–Dy2 and Dy1–O6–Dy2 are 110.5(3)° and 111.0(3)°, respectively.

bridging ligand ( $\mu_2\text{-}\eta^1\text{-}\eta^1$ ) between the two Dy<sup>III</sup> centers (Figure S10).

The defect cubane core  $[\text{Dy}_4(\mu_2\text{-O})_4(\mu_3\text{-OH})_2]^{6+}$  contains four coplanar metal centers, Dy1, Dy1\*, and Dy2, Dy2\* (Figure 5).

Overall, **2** contains two different types of eight-coordinate Dy<sup>III</sup> centers; one has a 7O, 1N coordination environment (Dy1) and the other has a 6O, 2N environment (Dy2). Both of these metal centers have been shown to possess a spherical capped square antiprism geometry by the SHAPE analysis program (Figure S11 and Table S4).<sup>15</sup>

The selected bond parameters are provided in the caption of Figure 4. The Dy–N bonds distances range from 2.528(7) to 2.669(7) Å, and the longest bond observed for Dy–N<sub>diethanolamine</sub> (Dy2–N4) is 2.629(7) Å. The observed average Dy–O<sub>CH<sub>2</sub>OH</sub> bond length is 2.415(5) Å and was found slightly longer than Dy–O<sub>hydrazone</sub> (2.354(5) Å). The average Dy–O<sub>piv</sub> bond length is 2.432(7) Å and is found to be slightly longer than the Dy–O<sub>hydrazone</sub> bond length. Then, the shortest distance among the Dy–O distances is found for Dy–O<sub>phen</sub> (Dy1–O1) to be 2.231(5) Å.

Analysis of the crystal packing diagram reveals that the shortest distance between two Dy<sup>III</sup> centers of the neighboring molecule is 9.155(1) Å (Figure S12).

The crystal structure of **2** reveals two pairs of intramolecular hydrogen bonds (O7\*–H3\*–O3\*, O7–H3–O3) and four CH $\cdots$ O interactions leading to the formation of a two-dimensional (2D) polymeric structure (Figures S13 and S14 and Tables S5 and S6).

The single-crystal X-ray diffraction study of **3** reveals that the homometallic hexanuclear complex is cationic with five chloride counterions (space group  $P2_1/n$  with  $Z = 4$ ). The asymmetric unit consists of the full molecule, *viz.*,  $[\text{Dy}_6(\text{H}_2\text{L})_3(\mu_3\text{-OH})(\mu_3\text{-CO}_3)_3(\text{CH}_3\text{OH})_4(\text{H}_2\text{O})_8]^{5\text{Cl}^-} 3\text{H}_2\text{O}$  (Figure 6). The molecular structure of **3** is provided

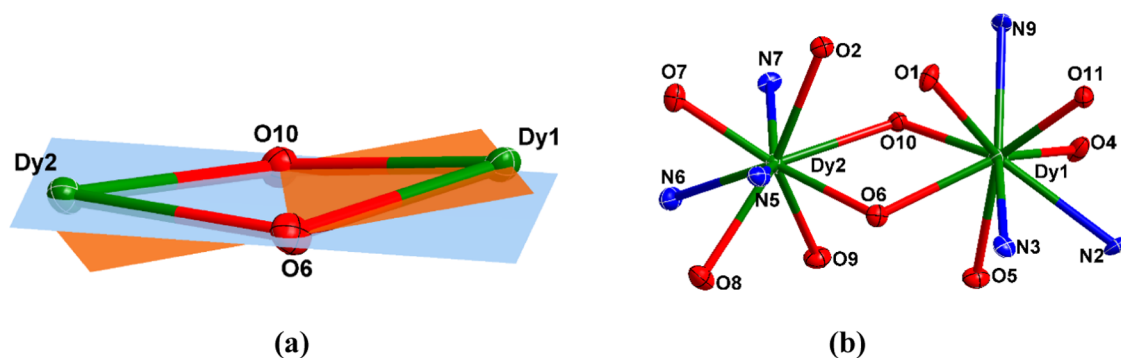


Figure 3. (a)  $Dy_2O_2$  core of **1**; (b) core structure of **1**. The outer backbone of the ligands is omitted for clarity.

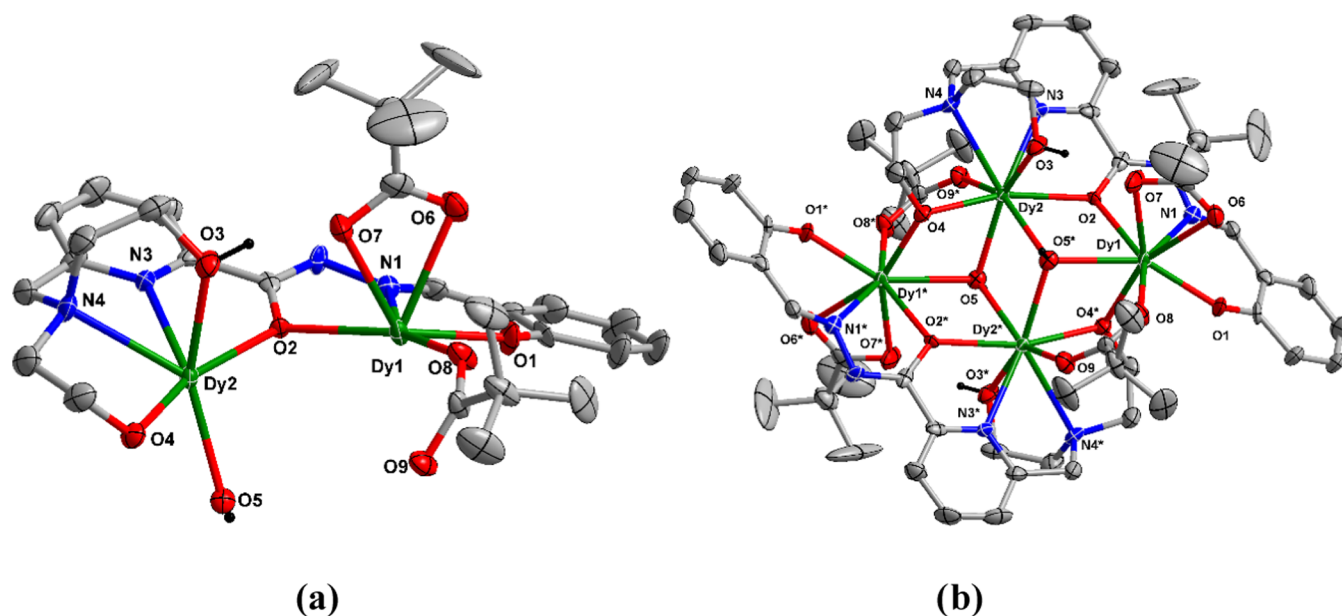


Figure 4. (a) Asymmetric unit of **2**, (b) Molecular structure of **2**. Thermal ellipsoids at a 50% probability level are shown (selected hydrogen atoms and the solvent molecules have been omitted for clarity). Color codes: N = blue; O = red; C = gray; Dy = dark green and H = black. Selected bond lengths (Å) for **2**: for Dy1; Dy1–O1, Dy1–O2, Dy1–O4\*, Dy1–O5\*, Dy1–O6, Dy1–O7, Dy1–O8, and Dy1–N1 are 2.230 (6), 2.368(5), 2.279(6), 2.432(6), 2.555(6), 2.438(6), 2.301(6), and 2.528(7), respectively, for Dy2; Dy2–O2, Dy2–O3, Dy2–O4, Dy2–O5, Dy2–O5\*, Dy2–O9, Dy2–N3, and Dy2–N4 are 2.343(5), 2.415(6), 2.248(5), 2.337(6), 2.343(6), 2.312(6), 2.535(7), and 2.635(7), respectively, and selected bond angles for **1**: Dy1–O2–Dy2, Dy1–O5–Dy2, Dy2–O5–Dy1\*, Dy2–O4–Dy1\*, and Dy2–O5–Dy2\* are 113.3(2)°, 111.1(3)°, 101.0(2)°, 109.0 (2)°, and 108.0(2)°, respectively.

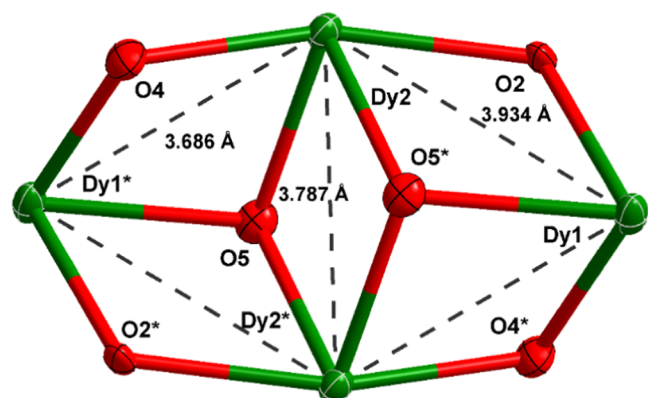


Figure 5. Butterfly-shaped tetranuclear core of **2**.

in Figure 6. Selected bond parameters are given in the caption of Figure 6, while others are given in the Supporting Information (Table S7).

The hexanuclear assembly **3** consists of three dinuclear subunits (Dy1/Dy4, Dy2/Dy5, Dy3/Dy6), each subunit being held together by  $[H_2L]^2$  in  $\mu_2-\eta^1:\eta^1:\eta^2:\eta^1:\eta^1:\eta^1:\eta^1$  manner (Figure S15).

Three such dinuclear subunits are stitched together by three carbonate ligands in a  $\mu_4-\eta^1:\eta^2:\eta^2$  manner and one  $[\mu_3-OH]^-$  to afford a propeller-shaped hexanuclear assembly (Figure 7).

The metal centers in the hexanuclear assembly are at the corners of two isosceles triangles [ $d_{Dy1-Dy2} = 3.999$  Å,  $d_{Dy2-Dy3} = 3.989$  Å,  $d_{Dy1-Dy3} = 3.975$  Å, and Dy4/Dy5/Dy6, where  $d_{Dy4-Dy5} = 6.206$  Å,  $d_{Dy5-Dy6} = 6.226$  Å,  $d_{Dy6-Dy4} = 6.224$  Å] (Figure 7b).

All of the Dy<sup>III</sup> centers are nine-coordinate. Three of these, Dy4, Dy5, and Dy6, have a 2N, 7O coordination environment while Dy1, Dy2, and Dy3 have a 1N, 8O coordination environment in a Muffin shape as determined by the SHAPE analysis program (Figure S16 and Table S1).<sup>15</sup>

As in the other complexes, the shortest Dy–O distance is observed for the coordination involving the phenolate oxygen

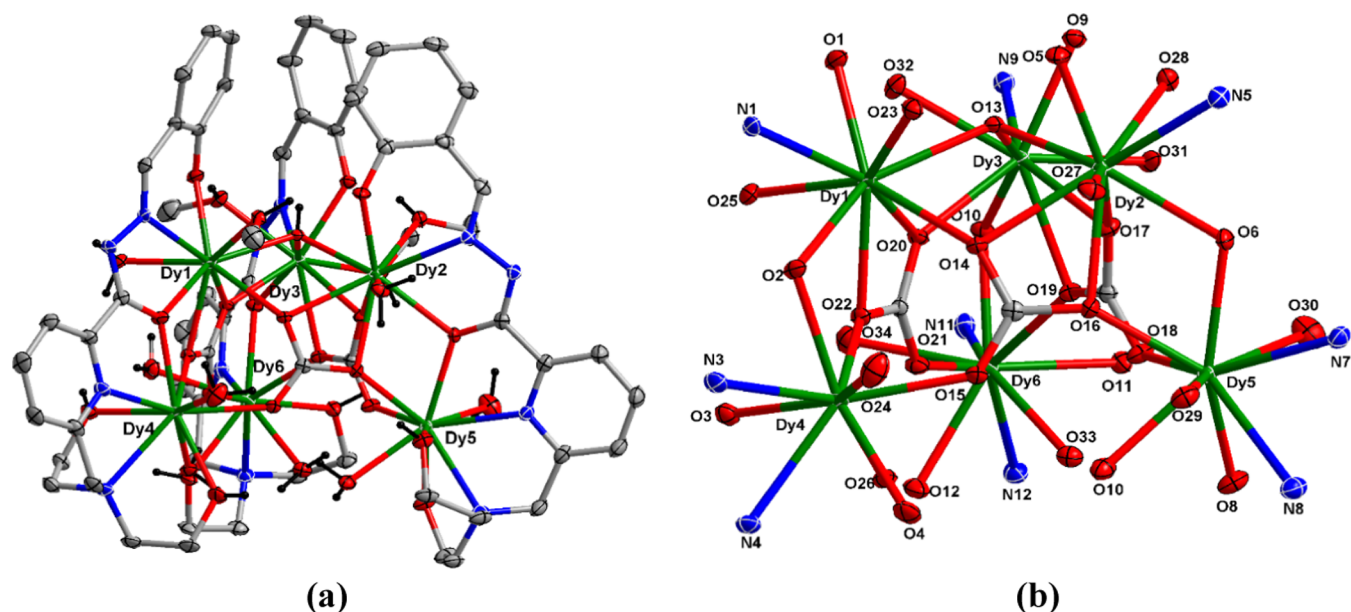


**Figure 6.** (a) Molecular structure of **3**, (b) Core of **3**. Thermal ellipsoids at a 50% probability level are shown (selected hydrogen atoms and the solvent molecules have been omitted for clarity). Color codes: N = blue; O = red; C = gray; Dy = dark green; H = black. Some selected shortest bond lengths (Å) for **3** around the metal centers: for Dy1; Dy1–O1<sub>phen</sub>, Dy1–O2<sub>enolato</sub>, Dy1–O13<sub>hydroxide</sub>, Dy1–O14<sub>carbonate</sub>, Dy1–O20<sub>carbonate</sub>, and Dy1–O22<sub>carboante</sub> are 2.2671(19), 2.3969(19), 2.439(2), 2.3710(19), 2.5017(19), and 2.4652(19), respectively, for Dy2; Dy2–O5<sub>phen</sub>, Dy2–O6<sub>enolato</sub>, Dy2–O13<sub>hydroxide</sub>, Dy2–O14<sub>carbonate</sub>, Dy2–O16<sub>carbonate</sub>, and Dy2–O17<sub>carboante</sub> are 2.2722(19), 2.4078(19), 2.427(2), 2.4992(19), 2.4575(19), and 2.3771(19), respectively, for Dy3; Dy3–O9<sub>phen</sub>, Dy3–O10<sub>enolato</sub>, Dy3–O13<sub>hydroxide</sub>, Dy3–O17<sub>carbonate</sub>, Dy3–O19<sub>carbonate</sub>, and Dy3–O20<sub>carbonate</sub> are 2.2606(19), 2.4001(19), 2.413(2), 2.4898(19), 2.4705(19), and 2.3552(19), respectively, for Dy4; Dy4–O2<sub>enolato</sub>, Dy4–O15<sub>carbonate</sub>, and Dy3–O22<sub>carboante</sub> are 2.3861(19), 2.3429(19), and 2.3467(18), respectively, for Dy5; Dy5–O6<sub>enolato</sub>, Dy5–O16<sub>carbonate</sub>, and Dy5–O18<sub>carbonate</sub> are 2.3919(19), 2.3407(18), and 2.357(2), respectively, for Dy6; Dy6–O10<sub>enolato</sub>, Dy6–O19<sub>carbonate</sub>, and Dy6–O21<sub>carbonate</sub> are 2.3927(19), 2.3571(19), and 2.3366(19), respectively.

atom. Some selected bond parameters are given in the caption of Figure 6 and Table S5.

Analysis of the crystal packing diagram reveals that the shortest distance between two Dy<sup>III</sup> centers of the neighboring molecule is 9.788(1) Å. (Figure S17).

The crystal structure of **3** reveals the presence of several intramolecular hydrogen bonds leading to the formation of a supramolecular structure (Figure S18 and Table S8).

**Magnetic Properties.** The temperature dependence of the magnetic susceptibility for **1–3** in the 2–300 K range and under a constant magnetic field of 0.1 T is shown in Figure 8 (left). At room temperature, the  $\chi_M T$  values for **1–3** of 28.80, 56.90, and 83.70 cm<sup>3</sup>·mol<sup>−1</sup>·K, respectively, are close to the expected values of 28.34, 56.7, and 85.02 cm<sup>3</sup>·mol<sup>−1</sup>·K for two, four and six Dy<sup>3+</sup> ions, respectively, in the free-ion approximation ( $J = 15/2$  and  $g = 4/3$ ). When lowering the temperature, the  $\chi_M T$  product for **1–3** remains nearly constant from room temperature to approximately 40, 45, and 70 K, respectively, whereupon it starts to decrease in a deeper manner reaching minimum values of 26.02, 32.94, and 50.29 cm<sup>3</sup>·mol<sup>−1</sup>·K, respectively, at 2 K. This decrease could be attributed to the thermal depopulation of the Kramers doublets arising from the splitting of the ground multiplet by crystal field effects and to the possible existence of intramolecular antiferromagnetic interactions between the Dy<sup>3+</sup> ions.

The isothermal magnetization curves measured at 2 K and up to 5 T for complexes **1–3** (Figure 8 (right)) show a relatively rapid increase in the magnetization at low field and almost saturation at high field (complex **3**, however, shows a linear increase of the magnetization at high field without achieving saturation at 5 T). This behavior suggests the

presence of a significant magnetic anisotropy and/or the presence of low-lying excited states that are partially populated at this temperature. The low-lying excited states are in agreement with weak magnetic interactions expected for these systems. It is worth noting that even though the  $\chi_M T$  vs  $T$  plot does not show a maximum at a very low temperature and the  $M$  vs  $H$  plot does not display an S shape, the second derivative of  $\chi_M T$  vs  $T$  plot and the first derivative of  $M$  vs  $H$  (see Figure S19), might be cautiously indicative of a nonmagnetic ground state, whose more patent effects should be observed below 2 K.

The magnetization values at the maximum applied field of 5 T are rather lower than those theoretically extracted from the free ion approximation (20, 40, and 60  $N\beta$  for **1–3**, respectively), which supports the presence of significant magnetic anisotropy due to crystal field splitting effects.<sup>6e,16,17</sup>

It is worth noting that the  $\chi_M' T$  product ( $\chi_M'$  is the in-phase ac susceptibility, Figure S20) for **1** at low temperature, where all of the lines are coincident, is 23.0 cm<sup>3</sup>·mol<sup>−1</sup>·K, which is not too far from that expected for randomly oriented crystals with a  $M_J = \pm 15/2$  Ising ground Kramer's doublet (25 cm<sup>3</sup>·mol<sup>−1</sup>·K). This fact is not unexpected as Dy<sup>III</sup> complexes with a nonsymmetric coordination environment, like **1**, generally exhibit an axial ground state (details are provided in the Theoretical Studies section). For instance, Dy<sup>III</sup> complexes with a Dy–O bond distance significantly shorter than the other Dy–donor distances possess an axial ground state with the anisotropic magnetic moment oriented along the shortest Dy–O direction.<sup>17</sup> This orientation can be easily understood considering that the f electron density of the  $m_J = \pm 15/2$  Dy<sup>III</sup> sublevels has an oblate shape. Because of this, and to reduce

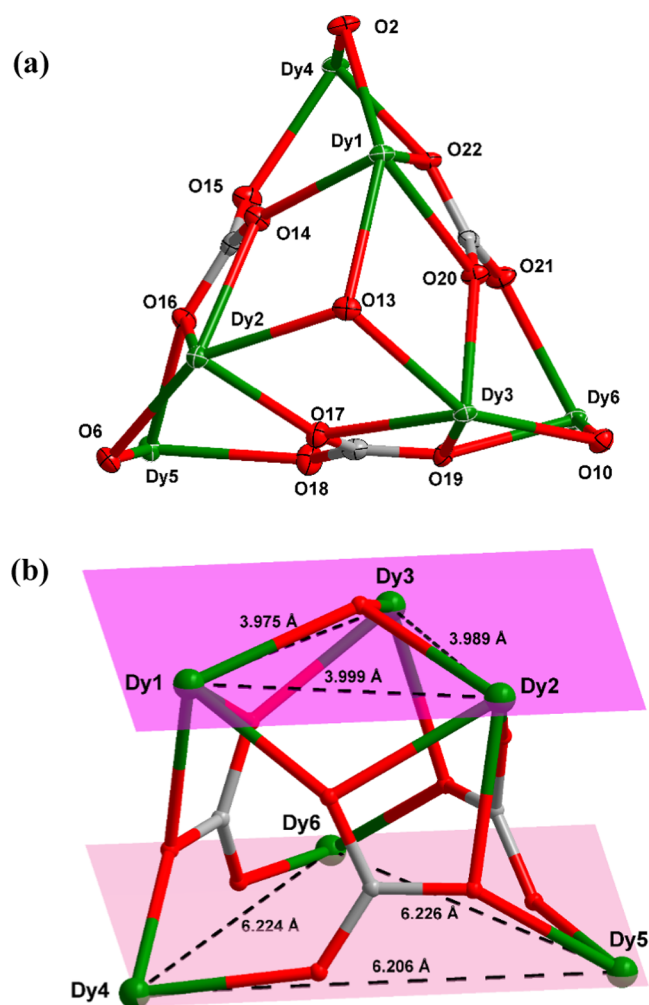


**Figure 7.** (a) View of propeller-shaped Dy<sub>6</sub> core; (b) view of the Dy<sub>6</sub> central core in two isosceles triangles in **3**.

the repulsion with the closest coordinated ligand donor atom (usually that possessing the largest electron density), the *f* electron density disk is accommodated almost perpendicular to the shortest Dy–O bond and then the magnetic moment is placed along this bond direction. This is the case of **1**, where the sole crystallographically independent Dy<sup>III</sup> ion shows a Dy–O<sub>phenoxide</sub> bond distance of 2.190 Å, which is rather shorter than the other ones in the 2.323–2.607 Å range. We have calculated the direction of the anisotropy axes of the Dy<sup>III</sup> ions

using the electrostatic Chilton's method and the Magellan software<sup>18</sup> and, as expected, the results show that the anisotropy axis on the twofold symmetrically related Dy<sup>III</sup> ions is located close to the Dy–O<sub>phenoxide</sub> bond (Figure S21), with an angle between their respective directions of 10.98°. The angle between the anisotropic axis and the molecular plane is 32.84°, whereas the angle between the line connecting the Dy<sup>III</sup> ions and the anisotropy axis is 60.8°.

It is worth noting that the main contribution to the magnetic coupling in oxo-bridged dinuclear Dy<sup>III</sup> complexes with short Dy...Dy distances of approximately 3.9 Å generally arises from the magnetic dipolar coupling rather than from exchange coupling. The dipolar contribution to the magnetic coupling can be calculated by the following equation for the energy of the dipole–dipole interaction<sup>17</sup>

$$E_{\text{dip}} = - \left\{ \frac{\mu_0}{4\pi} \right\} \frac{1}{r_{ij}^3} [3(\vec{\mu}_i \times \vec{\mu}_j) \cdot \vec{u}_{ij} - \vec{\mu}_i \times \vec{\mu}_j] \quad (1)$$

where  $u_{ij}$  is the unit vector connecting the interacting centers  $i$  and  $j$  and  $r$  is their distance;  $\mu_i$  and  $\mu_j$  are the magnetic moments of centers  $i$  and  $j$ ; and  $\mu_0$  is the vacuum permittivity. This expression leads to an antiferromagnetic coupling for angles between the magnetic moments and the molecular plane ( $\theta$ ) bigger than 66.2° and ferromagnetic coupling for angles lower than this value, respectively (for an angle value of 60.8° between the magnetic moments  $i$  and  $j$ , while the threshold angle value for a collinear system is 54.7°). In the case of **1**, the angle between the local magnetic moments of the ground state and the molecular plane (of 32.84°) (see Figure S21) determines the positive sign of the magnetic dipolar interaction. The estimated value of  $J_{\text{dip}}$  from eq 1 with the Hamiltonian  $H_{\text{dip}} = -J_{\text{dip}}J_{z1}J_{z2}$  (where  $J_{z1}J_{z2}$  represent the  $M_J$  values of the ground doublet state of the  $i$  and  $j$  centers) is +0.02 cm<sup>-1</sup>. In good accordance with this, the  $\chi_{\text{M}}T$  of **1** below 10 K is almost constant with a value of 26.5 cm<sup>3</sup>·mol<sup>-1</sup>·K (only shows a slight decrease below 2.5 K, Figure S22), which could be indicative of the existence of very weak ferromagnetic interaction between the Dy<sup>III</sup> ions. Thus, below 10 K, this very weak dipolar ferromagnetic interaction could balance the decrease in  $\chi_{\text{M}}T$  due to the depopulation of the  $M_J$  sublevels so that the  $\chi_{\text{M}}T$  would remain almost constant. The existence of a very weak magnetic interaction is not unexpected because the 4*f* orbitals of the Dy<sup>III</sup> are deeply buried into the atom and then very well shielded from the ligands by the 5*p* and 6*s* orbitals so that they have very little overlap with the bridging enolate oxygen atoms.

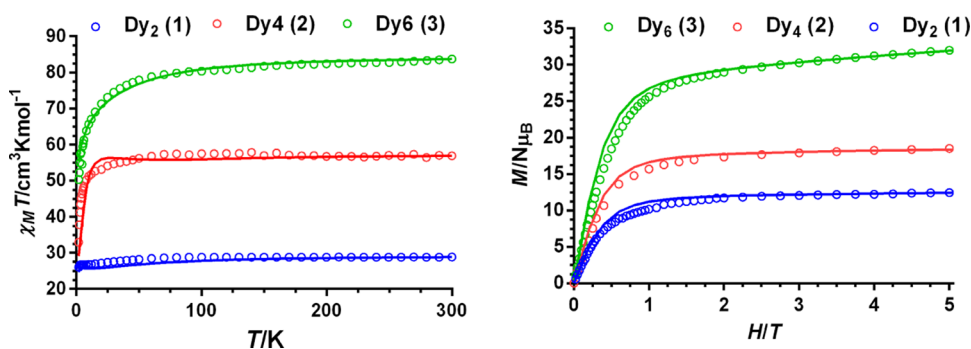


**Figure 8.** Temperature dependence of  $\chi_{\text{M}}T$  (left) and field dependence of the magnetization (right) for complexes **1–3**. Solid lines represent POLY\_ANISO fitted molar magnetic susceptibility vs  $T$  and  $M$  vs  $H$  curve.

**Table 2. Structural Parameters in the Dy<sub>2</sub>O<sub>2</sub> Bridging Core and Nature of the Magnetic Interactions for Some Dinuclear Dy<sup>III</sup> Complexes Containing Hydrazine-Enolate Multidentate Bridging Ligands**

complex	magnetic interaction	Dy...Dy (Å)	Dy–O (Å)	O–Dy–O (°)	coordination sphere	ref
[Dy <sub>2</sub> (NO <sub>3</sub> ) <sub>2</sub> (L <sub>1</sub> ) <sub>2</sub> (H <sub>2</sub> O) <sub>2</sub> ].2H <sub>2</sub> O	ferromagnetic	3.8258	2.348 2.319	110.1	N <sub>2</sub> O <sub>6</sub>	19a
[Dy <sub>2</sub> (NO <sub>3</sub> ) <sub>2</sub> (L <sub>2</sub> ) <sub>2</sub> (CH <sub>3</sub> OH) <sub>2</sub> ].4CH <sub>3</sub> CN	ferromagnetic	3.9225	2.319 2.313	114.9	N <sub>2</sub> O <sub>6</sub>	19b
[Dy <sub>2</sub> Cl <sub>2</sub> (H <sub>2</sub> L <sub>1</sub> ) <sub>2</sub> (MeOH) <sub>3</sub> ].CH <sub>3</sub> CN	ferromagnetic	3.8644	2.334 2.335 2.322 2.310	112.3 111.5	N <sub>2</sub> O <sub>3</sub> Cl <sub>2</sub> N <sub>2</sub> O <sub>6</sub>	7a
[Dy <sub>2</sub> (NO <sub>3</sub> ) <sub>4</sub> (L <sub>3</sub> ) <sub>2</sub> MeOH]		3.945	2.359 2.364	114.7 113.7	N <sub>4</sub> O <sub>6</sub> N <sub>2</sub> O <sub>7</sub>	19c
[Dy <sub>2</sub> (μ-NO <sub>3</sub> ) <sub>2</sub> (H <sub>2</sub> L) <sub>2</sub> ].[NO <sub>3</sub> ].2H <sub>2</sub> O		3.976	2.323 <sup>a</sup> 2.503 <sup>a</sup>	110.66	N <sub>3</sub> O <sub>6</sub>	this work

<sup>a</sup>Average values. H<sub>2</sub>L1: pyridine-2-carboxylic acid [(2-hydroxy-3-methoxyphenyl)methylene] hydrazide; L2: N'-2-((2-hydroxy-1-naphthyl)-methylene)picolinohydrazide; L3: N'-1-(pyridin-2-yl)ethylidene)pyridine-2-carbohydrazide; H<sub>4</sub>L: 6-((bis(2-hydroxyethyl)amino)-N'-(2-hydroxybenzylidene)picolinohydrazide).

Several examples of dinuclear Dy<sub>2</sub> complexes containing hydrazine-enolate multidentate bridging ligands, like that acting in **1**, have been reported so far.<sup>21</sup> In these complexes, the two enolate oxygen atoms bridge the Dy<sup>III</sup> centers to afford a rhombic Dy(O)<sub>2</sub>Dy bridging fragment (Table 2). All of these complexes present similar Dy–O, Dy–O–Dy, and Dy...Dy parameters in the bridging region with almost equal Dy–O distances within the Dy(O)<sub>2</sub>Dy fragment, and, with the exception of [Dy<sub>2</sub>(NO<sub>3</sub>)<sub>4</sub>(L<sub>3</sub>)<sub>2</sub>MeOH], exhibit ferromagnetic coupling. Although there is not a clear correlation between the sign of the magnetic coupling and the values of the bridging parameters, however, it seems that the combination of larger values of Dy–O, Dy–O–Dy, and Dy...Dy parameters in the bridging may favor weaker ferromagnetic interactions or even antiferromagnetic interactions. Thus, the complex [Dy<sub>2</sub>(NO<sub>3</sub>)<sub>3</sub>(L<sub>4</sub>)<sub>2</sub>MeOH] showing the greatest Dy–O, Dy–O–Dy, and Dy...Dy values presumably exhibits very weak antiferromagnetic interaction. Nevertheless, because the contribution to the magnetic coupling arising from the dipolar magnetic interactions in this type of Dy<sub>2</sub> complexes with Dy...Dy distances between 3.8 and 4 Å is rather larger than the magnetic exchange interaction, the Dy...Dy distance plays a more relevant role than the other bridging parameters. It is worth noting that, in good accordance with the above equation, when there is a near-parallel alignment of the local anisotropy axes and the line connecting the dysprosium ions ( $\theta = 0$ ), relatively stronger ferromagnetic dipolar interactions are expected. This is the case of complexes [Dy<sub>2</sub>(NO<sub>3</sub>)<sub>2</sub>(L<sub>1</sub>)<sub>2</sub>(H<sub>2</sub>O)<sub>2</sub>].2H<sub>2</sub>O,<sup>19a</sup> [Dy<sub>2</sub>(NO<sub>3</sub>)<sub>2</sub>(L<sub>2</sub>)<sub>2</sub>(CH<sub>3</sub>OH)<sub>2</sub>].4CH<sub>3</sub>CN,<sup>19b</sup> [Dy<sub>2</sub>Cl<sub>2</sub>(H<sub>2</sub>L<sub>1</sub>)<sub>2</sub>(MeOH)<sub>3</sub>].CH<sub>3</sub>CN,<sup>7a</sup> where the two shortest Dy–O distances are those corresponding to the phenoxido oxygen atoms coordinated almost in trans positions to the line connecting the Dy<sup>III</sup> ions. In such a disposition, the anisotropy axes align to the Dy–O<sub>phenoxo</sub> direction, which is near-parallel with the line connecting the Dy<sup>III</sup> centers. In the case of [Dy<sub>2</sub>(NO<sub>3</sub>)<sub>4</sub>(L<sub>3</sub>)<sub>2</sub>MeOH],<sup>19c</sup> however, the Dy–O distances are found in the 2.326–2.586 Å range so that the distribution of the charged oxygen atoms is rather spherical. In this case, the calculation of the orientation of the anisotropic axes using the Magellan program may be meaningless. Keeping it in mind, the results of the calculation indicate that the anisotropic axes are almost perpendicular to each other, which, together with

the large Dy...Dy distance, would lead to a ferromagnetic interaction much weaker than that observed in the other three complexes gathered in Table 2.

Compared to these four complexes, complex **1** presents the following important differences: (i) The Dy–O distances within the Dy(μ-O<sub>2</sub>)Dy bridging fragment are rather different and, moreover, one of them (of ~2.5 Å) is rather long. This further leads to a Dy...Dy distance that is larger than those observed in the other complexes given in Table 2. (ii) The anisotropic axes are not parallel to each other and with the line connecting the Dy<sup>III</sup> centers. (iii) There exists an additional nitrate ligand bridging the Dy<sup>III</sup> ions in a μ<sub>2</sub>-η<sup>1</sup>:η<sup>1</sup> manner. The nitrate bridging ligand is known to transmit very poor magnetic interactions in transition-metal complexes<sup>20</sup> and, therefore, much weaker interactions are expected in Dy<sup>3+</sup> nitrate-bridged complexes. In view of this, we will assume that the role played by the multiatomic nitrate bridge in transmitting magnetic exchange compared to the monoatomic enolate bridges, if any, is negligible. As for the differences (i) and (ii), both would reduce the magnitude of the exchange and dipolar contributions to the ferromagnetic coupling with regard to those expected for complexes [Dy<sub>2</sub>(NO<sub>3</sub>)<sub>2</sub>(L<sub>1</sub>)<sub>2</sub>(H<sub>2</sub>O)<sub>2</sub>].2H<sub>2</sub>O, [Dy<sub>2</sub>(NO<sub>3</sub>)<sub>2</sub>(L<sub>2</sub>)<sub>2</sub>(CH<sub>3</sub>OH)<sub>2</sub>].4CH<sub>3</sub>CN, [Dy<sub>2</sub>Cl<sub>2</sub>(H<sub>2</sub>L<sub>1</sub>)<sub>2</sub>(MeOH)<sub>3</sub>].CH<sub>3</sub>CN, which is in good accordance with the experimental results. Nevertheless, these conclusions about the nature and magnitude of the magnetic coupling in this type of alkoxide-bridged Dy<sub>2</sub> complexes should be taken with caution, as other factors such as the type and distributions of donor atoms in the Dy<sup>III</sup> coordination sphere are likely to affect magnetic coupling between the Dy<sup>III</sup> ions.

In view of the above considerations for complex **1**, it is clear that the magnetic coupling between the Dy<sup>III</sup> ions is very weak and hence the magnetic behavior should be single ion in origin. Moreover, as indicated above, the short Dy–O<sub>phenoxo</sub> distance anticipates an axial anisotropy of the ground state of the Dy<sup>III</sup> ion in **1**.<sup>17</sup> Consequently, it is probable that this compound exhibits slow relaxation of the magnetization and SMM behavior at zero magnetic field. To verify this, alternating current *ac* magnetic susceptibility measurements as a function of temperature and frequency were performed on complex **1**. The results show frequency-dependent maxima in the χ<sub>M</sub><sup>''</sup> signals below 10 K (see Figure 9) that overlap with a tail at a

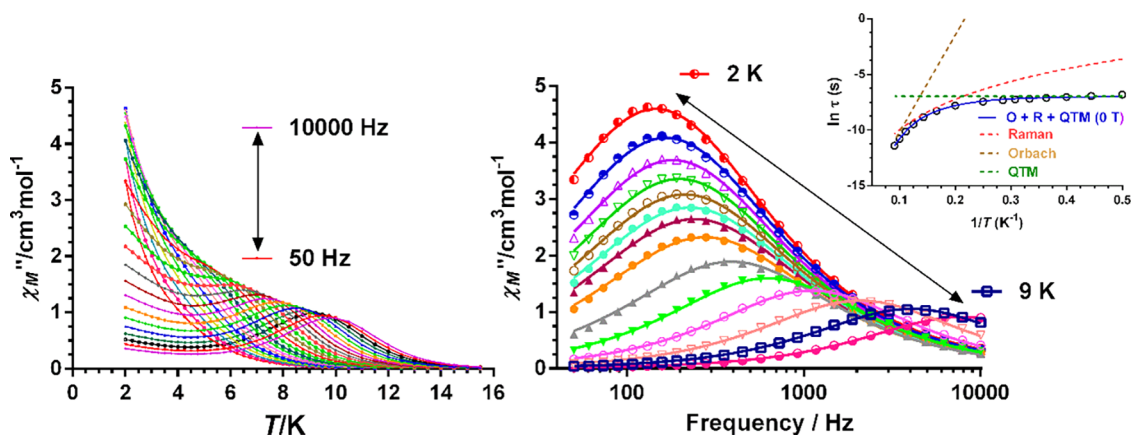


**Figure 9.** Temperature and frequency dependence of the out-of-phase  $\chi_M''$  susceptibility signals for complex **1** under zero field. The solid lines in the figure on the right-hand side represent the best fit to the generalized Debye model. Inset: Arrhenius plot for the relaxation times. The blue solid line accounts for the best fit considering the simultaneous presence of Orbach (brown dashed line) + Raman (red dashed line) + QTM relaxation processes (green dashed line).

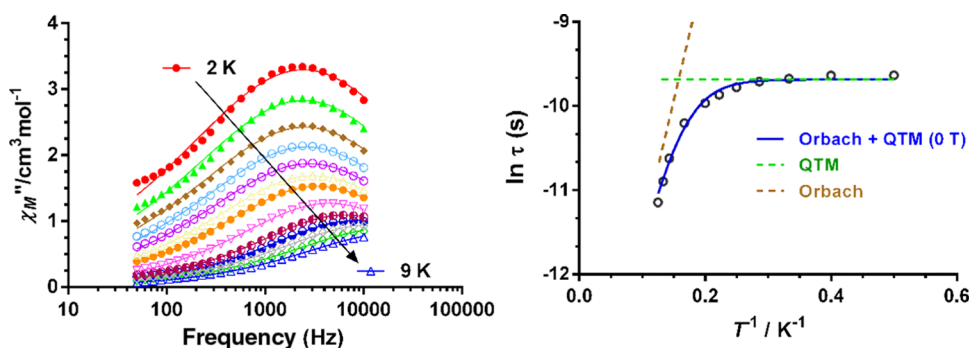


**Figure 10.** Frequency dependence of the out-of-phase  $\chi_M''$  susceptibility signals at different temperatures for complex **2** under zero field (left). The solid lines represent the best fit to the Debye model. Arrhenius plot for the relaxation times at 0 T (black circles). Solid lines account for the best fits considering the simultaneous presence of QTM (dashed green line) + Orbach (dashed brown line) (right).

low temperature ( $\chi_M''$  does not go to zero below the maxima but increases up to 2 K at low frequencies), thus confirming the existence of slow relaxation and SMM behavior at zero field.

The appearance of this tail suggests the existence of fast quantum tunneling of magnetization (QTM) at a very low temperature, which can arise from transverse anisotropy in the ground state, and from the transversal field created by dipole–dipole<sup>17,21</sup> and hyperfine interactions.<sup>21a,22</sup> The normalized Cole–Cole plot for **1** under zero field in the temperature range of 2–10 K (Figure S13) exhibits semicircular shapes, as expected for one relaxation mode, with low  $\alpha$  values in the range of 0.18 (2 K)–0.06 (10 K), thus supporting the existence of a relatively narrow distribution of relaxation processes. The low values of  $\chi_s/\chi T$  (in the range 0.007–0.1) indicate that more than 90% of the sample is able to relax slowly (Figure S23).

Below 5 K, both QTM and Raman could contribute to the magnetization relaxation (the field dependence of the relaxation time rules out the existence of a direct process), whereas above 5 K, only Raman and Orbach relaxation processes could be operative.

The values of the relaxation times ( $\tau$ ) at each temperature were extracted from the fitting of the frequency dependence of  $\chi_M''$  at different temperatures to the generalized Debye model. The temperature dependence of the relaxation times in the form of an Arrhenius plot (Figure 9, inset) shows, apart from

the linear portion in the high-temperature range (representative of a thermally activated process), a curvature for the intermediate temperatures and almost constant relaxation times below 3 K, this latter being indicative of QTM. Therefore, the relaxation times were fitted to the following equation

$$t^{-1} = BT^n + t_0^{-1} \exp(-U_{\text{eff}}/k_B T) + t_{\text{QTM}}^{-1} \quad (2)$$

which takes into account the simultaneous presence of Raman, Orbach, and QTM relaxation modes, respectively. The best fit afforded the following parameters:  $B = 2.4(9) \text{ s}^{-1} \text{ K}^{-3.9}$ ,  $n = 3.9$ ;  $\tau_0 = 6.4(3) \times 10^{-9} \text{ s}$ ,  $U_{\text{eff}} = 87(1) \text{ K}$ , and  $\tau_{\text{QTM}} = 0.0009(5) \text{ s}$ . This latter value is close to that extracted from the field dependence of the relaxation time at zero field of 0.0007(7) (Figure S24). Although a value of 9 is expected for Kramer's ions like  $\text{Dy}^{\text{III}}$ , however, when both acoustic and optical phonons are present, values between 2 and 7 can be considered reasonable.<sup>23</sup>

To fully or partly remove the QTM relaxation process, *ac* measurements on compound **1** were performed in the presence of an optimal small external dc field of 0.15 T (that inducing the slowest relaxation process). The value of the optimal field was extracted from the field dependence of the relaxation time at 3 K (see Figure S24). Under the optimal field, the low tail due to QTM relaxation has not been fully eliminated and/or an incipient field-induced relaxation process appears below 3.5 K (Figure S25). In good accordance with the latter suggestion

and the existence of multiple processes,  $\alpha$  values below 4 K are greater than the extracted ones under zero-applied magnetic field at the same temperatures (Figure S26). Nevertheless, temperature- and frequency-dependent well-defined maxima between 5 K (50 Hz) and 10 K (10 000 Hz) appeared for all of the used frequencies (Figure S25). The normalized Cole–Cole diagram for **1** under an applied field of 0.15 T in the temperature range of 5–9 K (Figure S26) exhibits semicircular shapes with  $\alpha$  values in the range of 0.18 (5 K)–0.08 (9 K), as expected for one relaxation mode. The very small values of the  $\chi_S/\chi_T$  ratio (0.005–0.02) indicate that almost the whole sample relaxes slowly at 1500 Oe.

The relaxation times, extracted from the fitting of the frequency dependence of  $\chi_M''$  at different temperatures to the Debye model, are plotted in the form of  $\ln \tau$  vs  $1/T$  in Figure S27. As it can be observed in this figure, apart from the linear region in the high-temperature range of the plot, a remarkable curvature appears for the intermediate and low-temperature regions, suggesting the presence of multiple relaxation processes. In view of this, the relaxation times were also fitted to eq 2. The best fitting led to the following parameters:  $B = 0.08(2) \text{ s}^{-1} \text{ K}^{-5.5}$ ,  $n = 5.5$ ;  $\tau_0 = 2.5(1) \times 10^{-9} \text{ s}$ ,  $U_{\text{eff}} = 101(3) \text{ K}$ , and  $\tau_{\text{QTM}} = 0.02(1) \text{ s}$ . As expected, the applied magnetic field induces a partial quenching of QTM and then a slowdown of this relaxation process, together with a concomitant increase of  $U_{\text{eff}}$ .

Dynamic ac measurements of complex **2** under zero field show frequency and temperature dependence of both in-phase ( $\chi_M'$ ) and out-of-phase ( $\chi_M''$ ) signals below 15 K, which can be indicative of slow relaxation of the magnetization and SMM behavior (Figures 10 and S28). The  $\chi_M''$  vs  $T$  plot at frequencies in the 50–1000 Hz range (Figure S28) displays a broad signal with incipient maxima around 9 K, which overlap with a high-intensity tail appearing at lower temperatures. Below 6000 Hz, maxima become shoulder of the low-temperature tail and finally disappear so that at low frequencies, the  $\chi_M''$  component steadily increases below 15 K (Figure S28). This behavior can be attributed to the overlapping of different relaxation processes, including a fast quantum tunneling relaxation. The normalized Cole–Cole plots at the zero applied dc field in the range of 2–9 K (Figure S29) show incomplete semicircles with a very wide distribution of relaxation times ( $\alpha$  values are in the range of 0.52–0.42, respectively), as expected for the occurrence of several overlapping processes. The relaxation fraction, characterized by  $1 - \chi_S/\chi_T$ , ranges from 0.07 to 0.17, point out that more than 80% of the sample is able to relax slowly.

The latter process would be responsible for the increase of  $\chi_M''$  below 4 K. To know whether or not this compound shows QTM, we have performed a study of the field dependence of the  $\chi_M''$  vs frequency plot at 3 K (Figure S30). The results show that the relaxation time for the low-temperature process increases with the increase of the magnetic field until 0.1 T and then remains constant (Figure S30). Therefore, at least in part, the tail at low temperature should be due to fast QTM. The  $\chi_M''$  vs  $f$  plot at zero field only displays wide maxima in the 1000–10 000 Hz region (Figure 10). These data were fitted to the generalized Debye model to extract the temperature dependence of the relaxation times (Figure 10 (right)), which shows the linear portion in the high-temperature region due to a thermally activated Orbach process, a curvature at intermediate temperatures and almost constant relaxation times below 3.5 K (Figure 10 (right), inset). The low-

temperature behavior points out the presence of QTM. Taking this into account, the ac data at zero applied dc field were fitted to the following equation

$$t^{-1} = t_0^{-1} \exp(-U_{\text{eff}}/k_B T) + t_{\text{QTM}}^{-1} \quad (3)$$

where the first term corresponds to an Orbach process and the second one to QTM. The best fit afforded the following parameters:  $\tau_0 = 4.2(1) \times 10^{-7} \text{ s}$ ,  $U_{\text{eff}} = 31(2) \text{ K}$ , and  $\tau_{\text{QTM}} = 0.000062(1) \text{ s}$ .

To try to eliminate at least partly QTM, ac measurements were carried out under the optimal dc field of 0.1 T. The results indicate that the  $\chi_M''$  vs  $T$  plot has not been essentially modified with respect to that observed at zero dc field (Figure S31). Therefore, either QTM has been weakly quenched or the tail at a low temperature is not due to QTM but to a thermally activated process with so small effective thermal energy barrier ( $U_{\text{eff}}$ ) that its maxima appear below 2 K. As expected, the  $\chi_M''$  vs  $f$  and the temperature dependence of the relaxation times plots under 0.1 T are very similar to those observed under zero dc field (Figures S32 and 10 (right)). The normalized Cole–Cole at 0.1 T in the 2–9 K (Figure S33) are similar to those at zero field, but the  $\alpha$  values are smaller (in the 0.45–0.25 range, respectively), probably as a result of the quenching of the QTM, and the relaxation fraction slightly decreases with  $\chi_S/\chi_T$  values in the 0.1–0.35 range. The temperature dependence of the relaxation times at 0.1 T was fitted to eq 3, which implies the assumption of the existence of Orbach and QTM processes. The best fitting procedure led to the following parameters:  $\tau_0 = 9(1) \times 10^{-7} \text{ s}$ ,  $U_{\text{eff}} = 28.8(9) \text{ K}$  and  $\tau_{\text{QTM}} = 0.00017(1) \text{ s}$ . Although the parameters are very similar to those extracted under zero-field, QTM is rather smaller, as expected. In this scenario, the thermally activated process should contain the relaxation processes arising from the two different crystallographic independent  $\text{Dy}^{\text{III}}$  centers and the exchange interaction between them should favor the QTM process, which is not eliminated even in the presence of an applied magnetic field. An alternative scenario would be that of considering that the intense tail at a low temperature is due to a thermally activated process and so the temperature dependence of the relaxation times under zero field was fitted to the following equation

$$t^{-1} = t_{01}^{-1} \exp(-U_{\text{eff}1}/k_B T) + t_{01}^{-1} \exp(-U_{\text{eff}2}/k_B T) + t_{\text{QTM}}^{-1} \quad (4)$$

where the first and second terms represent two different thermally activated processes and the third term represents the remaining QTM. The best fit allowed extracting the following parameters:  $\tau_{01} = 2(1) \times 10^{-7} \text{ s}$ ,  $U_{\text{eff}1} = 37(8) \text{ K}$ ,  $\tau_{02} = 5(6) \times 10^{-5} \text{ s}$ ,  $U_{\text{eff}2} = 8(4) \text{ K}$ , and  $\tau_{\text{QTM}} = 0.000067(9) \text{ s}$  (Figure S34). In this latter scenario, the low- and high-temperature overlapping processes appearing in the  $\chi_M''$  vs  $T$  plot could be assigned to each type of  $\text{Dy}^{\text{III}}$  ions that are present in the structure, Dy1 and Dy2, with DyNO7 and DyO6N2 coordination spheres. These  $\text{Dy}^{\text{III}}$  ions are rather different, not only due to their distinct coordination spheres, but, and most importantly, to the number and distribution of the shortest Dy–O distances (<2.3 Å). Thus, Dy1 has two shortest Dy–O distances, which implicate the phenoxide and one alkoxide oxygen atoms belonging to two different ligands of 2.229 and 2.283 Å, respectively, which form an angle of 83.71 Å. However, Dy2 only has one shortest Dy–O distance of

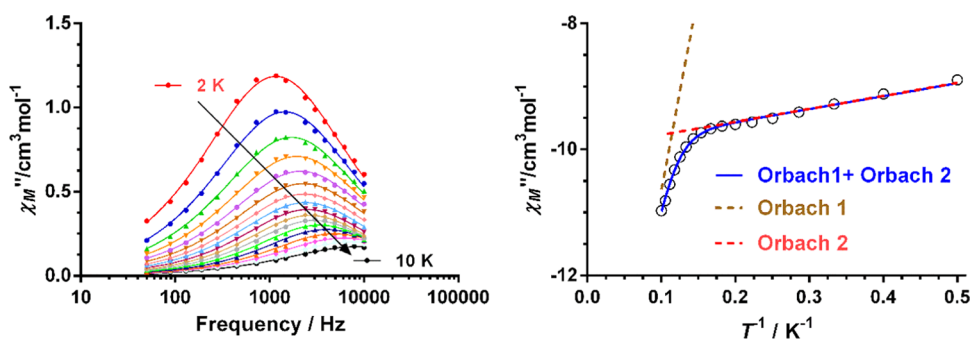


**Figure 11.** Frequency dependence of the out-of-phase  $\chi_M''$  susceptibility signals at different temperatures for complex 3 under zero field (left). The solid lines represent the best fit to the generalized Debye model. Arrhenius plot for the relaxation times at 0 T (blue circles). The black solid line accounts for the best fits considering the simultaneous presence of two Orbach relaxation processes (dashed red and brown lines).

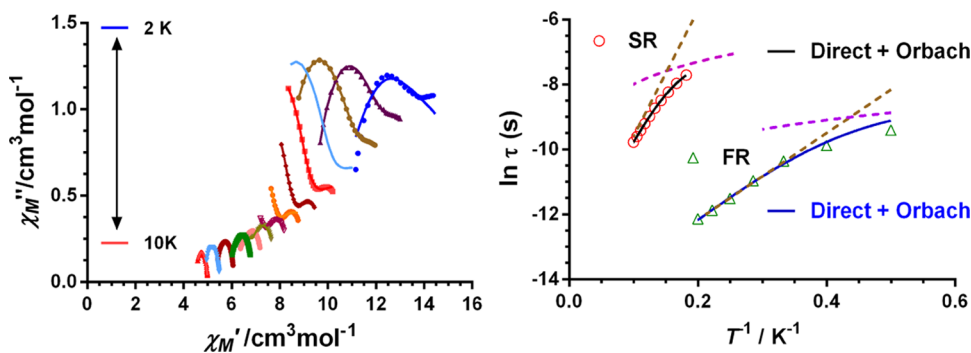


**Figure 12.** (Left) Cole–Cole plot for 3 under an applied field of 1200 Oe in the 2–10 K temperature range. Solid lines represent the best fits to the generalized Debye model. (Right) Arrhenius plot for the relaxation times at 1200 Oe of the FR (green triangles) and SR (red circles). The solid lines account for the best fits considering the simultaneous presence of direct (dashed violet line) + Orbach mechanisms (dashed brown line) for the FR process (blue) and SR process (green).

2.224 Å involving the alkoxide oxygen atom bridging Dy1 and Dy2. This situation, which is similar to that found in complex 1, is more favorable for the existence of an axial ground state than the disposition observed in Dy1, where the shortest Dy–O distances form almost a right angle. In light of this, Dy1 and Dy2 could be tentatively assigned to the lower- and higher-temperature processes, with small and high  $U_{\text{eff}}$  values, respectively.

It is worth mentioning that even though both interpretations of the ac data at 0.1 T for 2 appear to be reasonable, we feel, taking into account also the ac results for complex 3 (see below), that the second interpretation (two Orbach plus QTM) could be the most probable to occur.

Dynamic ac measurements of compound 3 at zero applied field indicate that  $\chi_M'$  and out-of-phase  $\chi_M''$  components of the susceptibility are frequency- and temperature-dependent below 15 K (Figures 11 and S35).

In this case, two clear maxima can be observed at  $\sim 4$  and  $\sim 10$  K above 4000 Hz, indicating the existence of two well-differentiated relaxation processes (Figure S35), which is not unexpected taking into consideration the existence of non-crystallographic equivalent  $\text{Dy}^{3+}$  in the asymmetric unit.<sup>24</sup> Nevertheless, below that frequency, both processes overlap and no maxima can be observed. The absence of maxima at low frequencies and low temperatures could be due to QTM and/or a thermal relaxation process with maxima appearing below 2 K. It should be noted that the frequency dependence of  $\chi_M''$  as well as the Cole–Cole plot at different temperatures (Figures 11 and S36) only show one relaxation process that must cover the two overlapping processes appearing in the  $\chi_M''$  vs  $T$  plot.

In line with this, the  $\alpha$  values are found in the 0.28–0.22 range. Moreover, the very high  $\chi_S/\chi_T$  values imply that almost 90% of the sample is not able undergo slow relaxation under zero field. In view of this, the  $\chi_M''$  vs  $f$  data at different temperatures were fitted to the generalized Debye model to extract the temperature dependence of the relaxation time for the sole observed process. Even though the field dependence of the relaxation times seems to indicate a contribution of QTM to the relaxation (see below), all attempts to fit the temperature dependence of the relaxation times including QTM failed in the low-temperature region. Therefore, the data were fitted to eq 2 for a combination of Raman and Orbach processes without considering the QTM term. The best fit led to the following parameters  $B = 0.01(1) \text{ s}^{-1} \text{ K}^{-6.6}$ ,  $n = 6.6(4)$ ;  $\tau_0 = 5(3) \times 10^{-5} \text{ s}$ , and  $U_{\text{eff}} = 1.8(3) \text{ K}$  (Figure S37). These parameters should correspond to the average of the two overlapping processes observed in  $\chi_M''$  vs  $T$  plot. Likewise, and to take into account that the low-temperature relaxation process could be due to an Orbach-type relaxation process, the temperature dependence of the relaxation times was fitted to a sum of two Orbach processes (eq 4 without considering the third term), leading to the following parameters:  $\tau_{01} = 4(1) \times 10^{-8} \text{ s}$ ,  $U_{\text{eff}1} = 62.4(3) \text{ K}$ ,  $\tau_{02} = 4.6(2) \times 10^{-5} \text{ s}$ , and  $U_{\text{eff}2} = 2.1(2) \text{ K}$ . In both scenarios, the low-temperature relaxation process exhibits, as expected, a very low value of  $U_{\text{eff}}$ .

The field dependence of the  $\chi_M''$  vs frequency plot (Figure S38) at 2.5 K clearly shows the presence of two relaxation processes. These data were fitted to a sum of two independent relaxation processes using the generalized Debye model and the CCFIT software,<sup>25</sup> which allowed the extraction of the

**Table 3.** *Ab Initio* Computed Energies of Low-Lying Eight KDs along with Ground- and First Excited-State *g*-Factors for Complexes 1–3

KD	complex 1		complex 2		complex 3					
	Dy-1	Dy-2	Dy-1/3	Dy-2/4	Dy-1	Dy-2	Dy-3	Dy-4	Dy-5	Dy-6
1	0.0	0.0	0.0	0.0	0.0	0.0	0.0	0.0	0.0	0.0
2	144.6	116.4	98.0	157.3	102.0	112.9	110.2	27.2	23.3	30.3
3	217.9	166.2	143.0	259.1	142.4	185.0	156.4	67.4	62.4	76.2
4	298.1	260.9	183.1	301.2	227.8	243.0	229.1	113.6	98.2	101.1
5	372.4	333.9	262.9	374.7	316.3	315.5	309.5	129.5	133.9	134.0
6	422.7	377.3	328.2	441.4	397.0	387.3	377.3	149.4	143.8	158.6
7	464.6	438.7	404.1	557.4	444.3	443.0	427.0	202.8	178.6	194.4
8	602.6	606.9	438.4	775.0	599.8	582.6	529.2	337.7	309.1	343.8
$g_{xx}$	0.030	0.059	0.083	0.004	0.080	0.052	0.067	0.337	10.923	1.803
$g_{yy}$	0.060	0.127	0.178	0.007	0.161	0.088	0.115	1.021	8.283	4.078
$g_{zz}$	19.658	19.437	19.616	19.863	19.347	19.425	19.446	17.750	2.352	15.110
$g_{xx}$	0.665	1.082	0.956	0.089	11.317	0.823	1.760	2.410	0.593	2.393
$g_{yy}$	1.434	3.089	1.825	0.127	7.589	1.403	4.399	4.410	3.476	5.324
$g_{zz}$	15.708	14.107	16.147	17.810	2.138	16.057	14.111	14.195	8.283	8.599

field dependence of the relaxation times for both processes. (Figure S38). The slow relaxation process, which is activated by the field, slows down with the increase of the field until reaching a maximum value at 1200 Oe, as would be expected if QTM were quenched. However, above 0.12 T, relaxation times sharply decrease, which could be due to a field-induced direct relaxation process, which depends on  $H^4$ . In fact, the field dependence of the relaxation times can be fitted to a sum of direct and QTM processes (Figure S38). The fast relaxation process, for which the relaxation time steadily decreases with the increase of the magnetic field, could not be fitted to a combination of QTM and direct processes. This behavior is more in line with the presence of hyperfine interactions, which depends on  $H^2T$ .<sup>21b</sup> As the relaxation time for the field-induced direct relaxation process (see above) is large at 1200 Oe, *ac* measurements were recorded under this optimal magnetic field, which clearly show in the  $\chi_M''$  vs  $T$  and  $\chi_M''$  vs  $f$  plots the presence of two set of maxima in the 2.5 K (50 Hz)–3.5 K (10 000 Hz) and 7.5 K (3000 Hz)–9.5 K (10 000 Hz) ranges (Figure S39). In the  $\chi_M''$  vs  $T$  plot, below 3000 Hz, the latter peaks overlap with those in the low-temperature region so that no clear maxima are observed in the high-temperature region. The Cole–Cole plot clearly exhibits the two relaxation processes, and therefore, these data were fitted to the sum of two independent processes using the CCFIT software,<sup>25</sup> allowing extracting the temperature dependence of the relaxation times for the fast (FR) and the slow (SR) relaxation processes (Figure 12). The extracted  $\tau$  vs  $T$  data for the FR process were fitted to a combination of direct and Orbach processes (eq 5)

$$\tau^{-1} = AT + t_0^{-1} \exp(-U_{\text{eff}}/k_B T) \quad (5)$$

where the first term corresponds to the direct relaxation process. The best fit afforded the following parameters:  $A = 3(4) \times 10^3 \text{ s}^{-1} \text{ K}$ ,  $\tau_0 = 2.8(9) \times 10^{-7} \text{ s}$ , and  $U_{\text{eff}} = 15.(2) \text{ K}$ . It should be noted that the fits to Raman plus Orbach, Raman plus direct, and even only Raman processes were rather worse than the Orbach plus direct processes.

The SR process was also fitted to a sum of direct and Orbach processes, leading to the following parameters:  $A = 296(7) \text{ s}^{-1} \text{ K}$ ,  $\tau_0 = 1.4(6) \times 10^{-6} \text{ s}$ , and  $U_{\text{eff}} = 38.9(3) \text{ K}$ . The normalized Cole–Cole plot (Figure S40) shows that the FR and SR relaxation processes have  $\alpha$  values in the ranges of 0.13

(2 K)–0.18 (3.5 K) and 0.40 (6 K)–0.26 (10 K), respectively, in good accordance with the existence of a wide distribution of relaxation times. Furthermore, at a low temperature, about half of the sample slowly relaxes through the FR process, whereas only almost 20% of the sample is able to relax through the SR at a high temperature. We have also measured the *ac* magnetic susceptibility under a field of 1900 Oe because at this field, the FR process is close to its maximum intensity value. As it can be seen in Figures S41–S43, the behavior under 1900 Oe is very similar to that under 1200 Oe (fitting parameters are given in the figure captions). The most important difference is that the SR process at 1900 Oe is slightly faster than at 1200 Oe.

We have also explored the possibility of Raman and Orbach contributions to the SR process, but in both cases (1200 and 1900 Oe), the fits are worsened and the power coefficient of the Raman process is close to  $n = 1$  (the expected value for the direct process).

Complex 3 presents two sets of Dy<sup>III</sup> ions concerning to the Dy-donor distances. The first set comprises Dy1, Dy2, and Dy3 ions. Each of these ions contains only one Dy–O<sub>phenoxido</sub> bond with the shortest Dy–O distance, which are in the 2.248–2.263 Å range, respectively. The rest of the distances in each coordination sphere are greater than 2.4 Å. The second set of Dy ions, Dy4, Dy5, and Dy6, do not contain any coordinated phenoxido group so that the shortest Dy–O distances involve the enolate and  $\mu_3$ -nitrate oxygen atoms, which are found in the 2.345–2.394 Å range. As for the first set of Dy ions, the rest of Dy-donor distances are all greater than 2.4 Å. As in the case of 1 and 2, the shortest Dy–O<sub>phenoxido</sub> distances cause large crystal effects and a stronger anisotropy. Thus, in the first case, a largely axial ground state relatively well separated from the excited states is expected, whereas in the second case a less axial ground state with not so well energy separation from the excited state could be assumed. The existence of these two sets of Dy ions could be the reason why two set of peaks are observed for compound 3 at different temperatures. If so, the first set should correspond to the relaxation process appearing at higher temperatures in the  $\chi_M''$  vs  $T$  plot, whereas the second set with shortest Dy–O distances larger than 2.35 Å should correspond to the relaxation process observed at lower temperatures.

**Theoretical Studies.** To understand the magnetic relaxation dynamics and the different relaxation processes

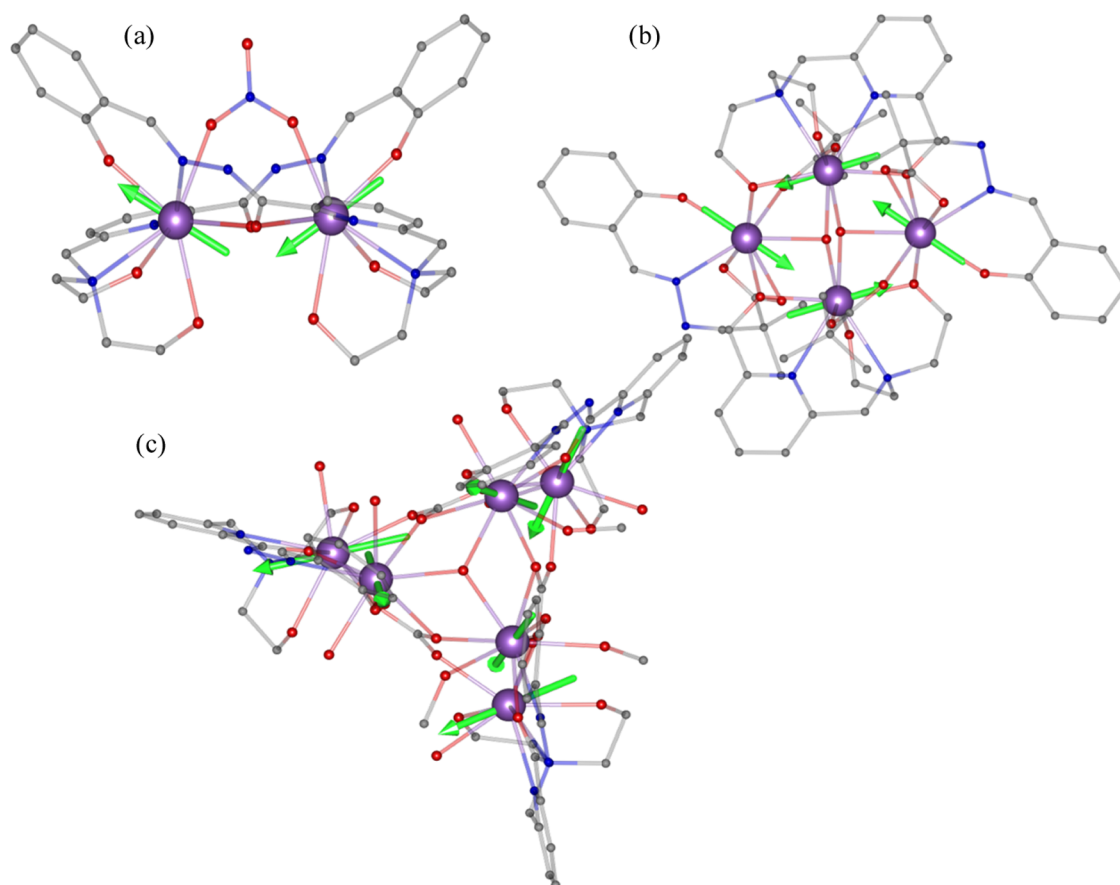


**Figure 13.** Arrangement of  $g_{zz}$  anisotropic axis for the ground-state KDs doublets of complexes (a) 1, (b) 2, and (c) 3. The green arrows indicate the alignment of anisotropic axis. Violet = Dy, gray = C, red = O, blue = N. Hydrogen atoms were omitted for clarity.

offered by the dinuclear(1), tetranuclear(2), and hexanuclear (3) Dy complexes, *ab initio* CASSCF/RASSI-SO/SINGLE\_-ANISO/POLY\_ANISO calculations have been performed on the crystal structures of the complexes obtained from the X-ray diffraction using the MOLCAS package. All of the calculations have been performed in two steps; first, the single-ion anisotropy has been derived for the individual Dy<sup>III</sup> centers, and then we proceed to the polynuclear complex using the input from the single-ion calculations.

**Mechanism of Magnetization Relaxation Originating from Single Ions.** The energies of low-lying eight Kramers Doublet (KD) originating from the  ${}^6H_{15/2}$  for individual Dy<sup>III</sup> for all three complexes are provided in Table 3, along with the ground- and first-excited-state  $g$  anisotropy values. It is worth noting that, for complex 1, both the Dy<sup>III</sup> ions are asymmetric and offer different ligand fields. Although both the Dy-1 and Dy-2 centers have  $\{DyO_6N_3\}$  moiety, the geometrical parameters are very different (see Figures 2, 4, and 6; Tables S1 and S4 in the SI). The ligand field is more axial for the Dy-1 center compared to the Dy-2 center, and hence the ground- to first-excited-state energy splitting is larger for the former than the latter (144.6 vs 116.4  $cm^{-1}$ ). This is reflected in the crystal field parameters  $B_2^0$ , which is larger for Dy-1 than for Dy-2 ( $-2.45$  for Dy-1 and  $-2.21$  for Dy-2, Table S10).<sup>26</sup>

For Dy-1, the ground-state anisotropy is purely Ising in nature ( $g_{zz} = 19.658$ ,  $g_{xx} = 0.03$ ,  $g_{yy} = 0.06$ ), whereas for Dy-2, a small transverse anisotropy is present in the ground state ( $g_{zz} = 19.437$ ,  $g_{xx} = 0.06$ ,  $g_{yy} = 0.13$ ). The ground state is estimated to be  $m_j = \pm 15/2$  for both of the centers, and a strong mixing is

observed in the first excited state. This is reflected in their  $g$  anisotropy (see Table 3). For both centers, the single-ion relaxation is taking place in the first excited via Raman/Orbach or TA-QTM process (see Figure 14). The ground-state anisotropy axis arrangement for each of the Dy<sup>III</sup> centers is plotted in Figure 13, which agrees with the direction predicted from the electrostatic model and is based on the shortest Dy–O bond lengths.<sup>18</sup> In fact, the average angle between the anisotropic axis and the molecular plane is  $31.5^\circ$  and the angle between the line connecting the Dy<sup>III</sup> ions and the anisotropy axis is  $59.0^\circ$ , which are both very close to those extracted from the electrostatic model.

For complex 2, the two Dy<sup>III</sup> centers at the wing part (Dy-1 and Dy-3) and two Dy<sup>III</sup> centers at the body part (Dy-2 and Dy-4) of the inverse butterfly core are symmetric with respect to each other and exhibit the same single-ion anisotropy. The wing Dy-1 and Dy-3 centers have  $\{DyO_7N\}$  coordination mode, while the body Dy-2 and Dy-4 centers have  $\{DyO_6N_2\}$  coordination from the ligands. Hence, the LoProp charge and the crystal field parameters around the corresponding Dy<sup>III</sup> centers differ dramatically (Table S9 and Figure S44 in the SI), resulting in ground first-excited-state KD energy gaps of 98.0  $cm^{-1}$  ( $B_2^0 = -1.58$ ) and 157.3  $cm^{-1}$  ( $B_2^0 = -2.42$ ) for Dy-1/3 and Dy-2/4, respectively. For the Dy-2/4 centers (highly axial,  $g_{zz} = 19.863$ ,  $g_{xx} = 0.004$ ,  $g_{yy} = 0.007$ ), the relaxation occurs via the second excited state, whereas for the Dy-1/3 (comparatively less axial  $g_{zz} = 19.616$ ,  $g_{xx} = 0.08$ ,  $g_{yy} = 0.18$ ) centers, it occurs via the first-excited state (see Figure 14, Table 3). The individual  $g$  anisotropy axes for each of the Dy<sup>III</sup> centers for

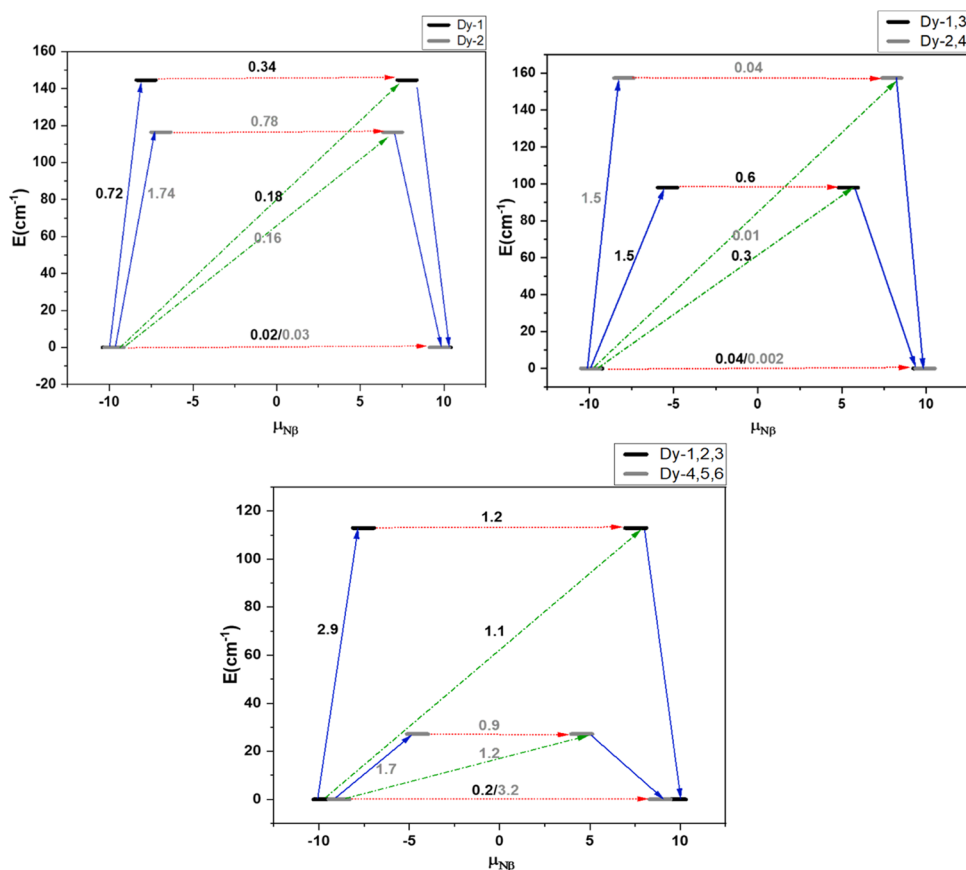


**Figure 14.** Magnetic relaxation dynamics through *ab initio* computation for each of the Dy centers for complexes 1, 2, and 3 (clockwise). The thick black line represents Kramer's doublets as a function of the computed magnetic moment. The green dotted arrows show the possible pathway through Orbach/Raman relaxation; dotted red lines and blue represent the presence of QTM/TA-QTM between the connecting pairs. The numbers provided at each arrow are the mean absolute value for the corresponding matrix element of the transition magnetic moment.

complex 2 are plotted in Figure 13. The direction of the ground state  $g_{zz}$  axes indicates a circular arrangement and suggests the possibility of observing toroidal moments. The probable S-shape behavior observed in the  $M$  vs  $H$  plot further suggests that this complex may exhibit toroidal moments.<sup>9a</sup>

Similarly, for complex 3, the three Dy<sup>III</sup> centers in the upper triangle structurally resemble each other, and the three Dy<sup>III</sup> of the lower triangle structurally resemble each other. For the upper triangle, all of the three Dy<sup>III</sup>(Dy-1/2/3) have {DyO<sub>7</sub>N} coordination mode, and for the lower triangle Dy<sup>III</sup>(Dy-4/5/6), {DyO<sub>7</sub>N<sub>2</sub>} coordination mode was observed. This difference in the coordination number and geometry strongly influences the anisotropy of the metal ions. The Dy<sup>III</sup> centers at the upper (Dy1–3) triangles show a ground-state first-excited-state KD energy gap in the range of 102–113  $\text{cm}^{-1}$ . The ground state is found to be axial ( $g_{zz} = 19.447$ – $19.347$ ,  $g_{xx} = 0.05$ – $0.08$ ,  $g_{yy} = 0.08$ – $0.18$ ; see Table 3). For the lower triangle, all of the Dy<sup>III</sup> ions exhibit a very large transverse anisotropy in the ground state with the ground-state first-excited-state KD energy gap estimated to be in the range of 23–30  $\text{cm}^{-1}$  (Table 3). For all of the six individual Dy<sup>III</sup> centers, the relaxation is taking place via the first-excited state (Figure 14). For both the triangles in complex 3, a circular arrangement of the anisotropic axes is absent, and therefore no toroidal moments are expected for this complex.

Despite the presence of strong anisotropy in the ground state and significantly less QTM in the ground state, the observed  $U_{\text{eff}}$  values for all three complexes are comparatively

less than the single ion obtained values for complex 1 (Dy<sub>2</sub>,  $U_{\text{eff}} = 60.2 \text{ cm}^{-1}$ ,  $U_{\text{calDy-1}} = 144.6 \text{ cm}^{-1}$ ,  $U_{\text{calDy-2}} = 116.4 \text{ cm}^{-1}$ ) and 2 (Dy<sub>4</sub>,  $U_{\text{eff}} = 21.5 \text{ cm}^{-1}$ ,  $U_{\text{calDy-1/3}} = 98 \text{ cm}^{-1}$ ,  $U_{\text{calDy-2/4}} = 157.3 \text{ cm}^{-1}$ ). For complex 3, the computed values found to lie on both ends compared to experiments (Dy<sub>6</sub>,  $U_{\text{eff}} = 43 \text{ cm}^{-1}$ ,  $U_{\text{calDy-1/2/3}} = 23.3$  to  $30.3 \text{ cm}^{-1}$ ,  $U_{\text{calDy-4/5/6}} = 102$  to  $112.9 \text{ cm}^{-1}$ ). The discrepancy between calculated and experimental energy barrier values is usual and can be ascribed to the inherent limitations of SINGLE\_ANISO routine, which does not consider intra- and intermolecular interactions, as well as to possible small structural changes at low temperatures.

To understand the role of exchange coupling in magnetization relaxation, we turn to the POLY\_ANISO method.

**Mechanism of Magnetization Relaxation Originating from the Exchange-Coupled States and Observance of SMT Behavior in 2.** The Dy–Dy centers coupling through the oxo bridges often results in weak but non-negligible exchange interactions. For complex 1, there is a single exchange interaction between the Dy–Dy centers mediating via two  $\mu$ -O enolate and via a  $\text{NO}_3^-$  bidentate bridging group, and for complex 2, four different exchange interactions were possible between the Dy1–Dy2, which is equal to Dy3–Dy4 interactions ( $J_1$  mediates via two  $\mu$ -O atom belonging to a  $\mu_3$ -OH and  $\mu$ -enolate groups and a carboxylate bridging group of the pivalate ligand; see Figure 15). Similarly, the exchange coupling between the Dy1–Dy4 and Dy2–Dy3 is estimated to be identical, and this is termed  $J_2$  mediating via a  $\mu_3$ -OH and an enolate bridging group (see Figure 15). The  $J_3$  and  $J_4$

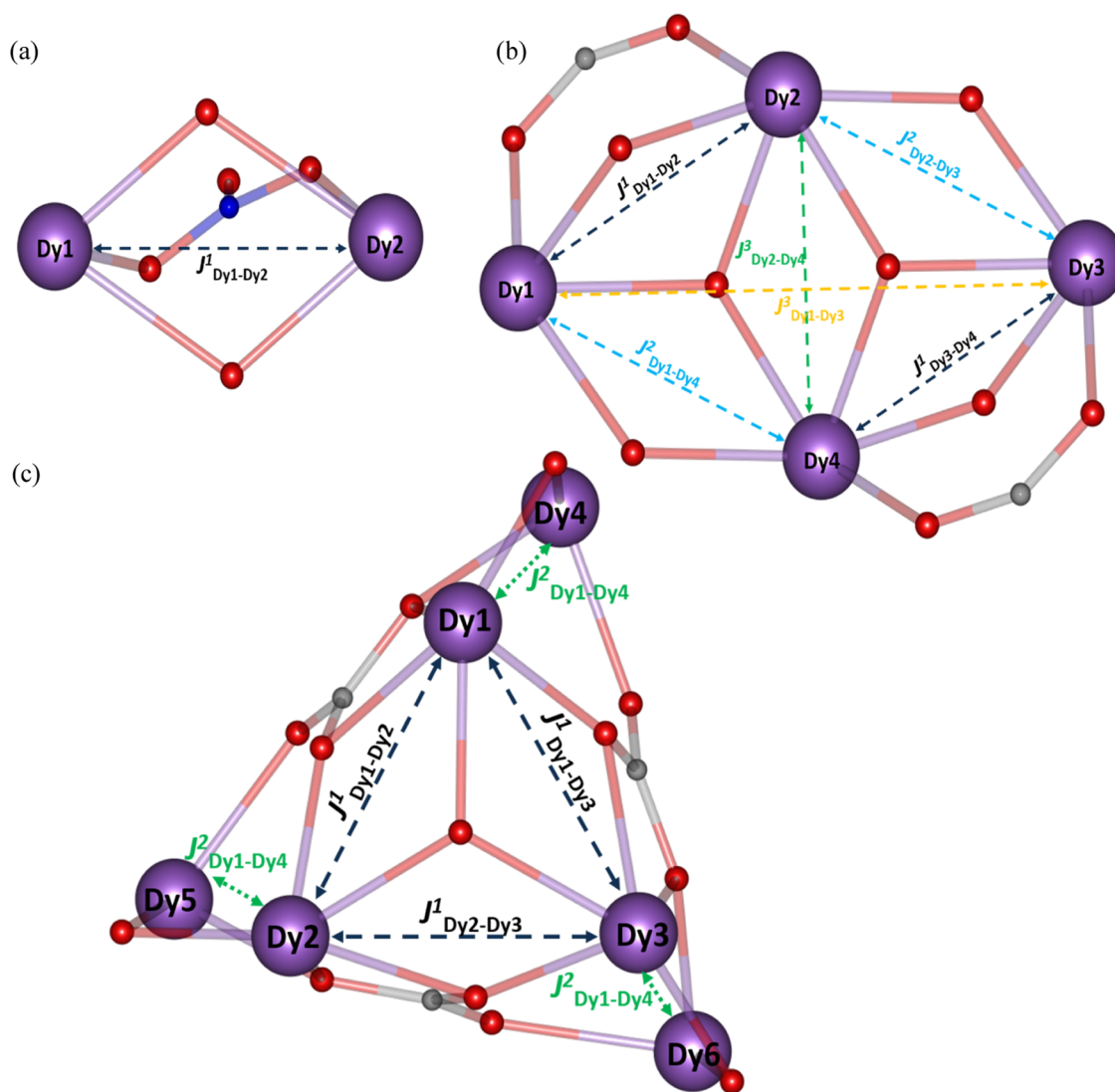


**Figure 15.** Different modes of exchange coupling between the Dy–Dy centers for three complexes, (a) 1-Dy2, (b) 2-Dy4, and (c) 3-Dy6).

**Table 4.** DFT-Computed and POLY\_ANISO Fitted Exchange Coupling Parameters for Complexes 1, 2, and 3<sup>a</sup>

complex	1-Dy2	2-Dy4	3-Dy6
$J_{Dy1-Dy2}^1$	$-0.021(J_{\text{dip}} = +0.03, J_{\text{tot}} = +0.009)$ [−0.02]	$-0.05(J_{\text{dip}} = +0.055, J_{\text{tot}} = +0.005)$ [−0.04]	$-0.01(J_{\text{dip}} = +0.04, J_{\text{tot}} = -0.03)$
$J_{Dy1-Dy4}^2$		$-0.006(J_{\text{dip}} = +0.02, J_{\text{tot}} = -0.014)$ [−0.01]	$-0.02(J_{\text{dip}} = +0.05, J_{\text{tot}} = -0.04)$
$J_{Dy2-Dy3}^2$		$-0.01(J_{\text{dip}} = +0.02, J_{\text{tot}} = -0.014)$ [−0.01]	$-0.01(J_{\text{dip}} = +0.04, J_{\text{tot}} = -0.03)$
$J_{Dy3-Dy4}^1$		$-0.04$ ( $J_{\text{dip}} = +0.045, J_{\text{tot}} = +0.005$ ) [−0.05]	
$J_{Dy2-Dy4}^3$		$-0.01(J_{\text{dip}} = +0.02, J_{\text{tot}} = -0.014)$ [−0.01]	
$J_{Dy1-Dy3}^3$			$-0.01(J_{\text{dip}} = +0.04, J_{\text{tot}} = -0.03)$
$J_{Dy2-Dy5}^2$			$-0.02(J_{\text{dip}} = +0.05, J_{\text{tot}} = -0.04)$
$J_{Dy3-Dy6}^2$			$-0.02(J_{\text{dip}} = +0.05, J_{\text{tot}} = -0.04)$

<sup>a</sup>\*The value in square brackets is obtained from the density functional calculations.

interactions between Dy1–Dy3 and Dy2–Dy4 mediate via two  $\mu_3$  oxo and long ligand spacer atoms, respectively. We have considered two different exchange interactions for complex 3:  $J_1$  via the  $\mu_3$ -OH group and  $\mu_3$ -OCO<sub>2</sub> group for the Dy1–3 in the upper triangle and  $J_2$  via  $\mu$ -O<sub>enolate</sub> and  $\mu_3$ -OCO<sub>2</sub> between the Dy centers of two triangles (Dy1–Dy4, etc.; Figure 15).

First, the exchange coupling has been estimated using the density functional theory (DFT) calculations by replacing the

anisotropic Dy<sup>III</sup> ion with the isotopic Gd<sup>III</sup> and rescaling it by a factor of 5/7 (see the Computational Details section) using the following Hamiltonian represented in eqs 6–8.<sup>27</sup> This exchange has been used as a starting guess for the POLY\_ANISO fitting to derive the magnetic relaxation dynamics for the overall complexes. A simultaneous fit for both susceptibility and magnetization data was performed (solid lines in Figure 8). The Dy···Dy dipolar coupling as

estimated using eqs 9 and 10 has been employed for our calculations. The exchange coupling obtained from the density functional calculations and *ab initio* POLY\_ANISO fitted values are provided in Table 4, which are in good agreement with each other. All of the calculated exchange couplings are in a similar range for Dy–Dy coupling.

For 1-Dy<sub>2</sub>

$$\hat{H}_{\text{exch}} = -J_{\text{Dy1-Dy2}} \hat{S}_{\text{Dy1}} \hat{S}_{\text{Dy2}} \quad (6)$$

For 2-Dy<sub>4</sub>

$$\begin{aligned} \hat{H}_{\text{exch}} = & -J_{\text{Dy1-Dy3}} \hat{S}_{\text{Dy1}} \hat{S}_{\text{Dy3}} - J_{\text{Dy2-Dy4}} \hat{S}_{\text{Dy2}} \hat{S}_{\text{Dy4}} \\ & - 2J_{\text{Dy1-Dy2}} \hat{S}_{\text{Dy1}} \hat{S}_{\text{Dy2}} - 2J_{\text{Dy1-Dy4}} \hat{S}_{\text{Dy1}} \hat{S}_{\text{Dy4}} \end{aligned} \quad (7)$$

For 3-Dy<sub>6</sub>

$$\begin{aligned} \hat{H}_{\text{exch}} = & -J_{\text{Dy1-Dy3}} \hat{S}_{\text{Dy1}} \hat{S}_{\text{Dy3}} - J_{\text{Dy2-Dy3}} \hat{S}_{\text{Dy2}} \hat{S}_{\text{Dy3}} \\ & - J_{\text{Dy1-Dy3}} \hat{S}_{\text{Dy1}} \hat{S}_{\text{Dy3}} - J_{\text{Dy1-Dy4}} \hat{S}_{\text{Dy1}} \hat{S}_{\text{Dy4}} \\ & - J_{\text{Dy2-Dy5}} \hat{S}_{\text{Dy2}} \hat{S}_{\text{Dy5}} - J_{\text{Dy3-Dy6}} \hat{S}_{\text{Dy3}} \hat{S}_{\text{Dy6}} \end{aligned} \quad (8)$$

The total exchange is the combination of both  $J_{\text{exch}}$  and  $J_{\text{dip}}$  using the following equation

$$\hat{H} = -\left(-J_{\text{dip}}^{L_n^i - L_n^{i+1}} + J_{\text{exch}}^{L_n^i - L_n^{i+1}}\right) \tilde{s}_{L_n^i} \tilde{s}_{L_n^{i+1}} \quad (9)$$

$$J_{\text{dip}}^{L_n^i - L_n^{i+1}} = \frac{\mu_B^2}{R_{\text{Dy}^i - \text{Dy}^{i+1}}^3} g_{L_n}^2 \quad (10)$$

The exchange coupling in Dy–Dy in complex 1 is found to be weakly ferromagnetic in nature (spin densities are given in Figure S45 for 1 and 2), whereas the dipolar coupling between the two centers exhibits relatively larger ferromagnetic coupling. The dipolar coupling computed with the POLY\_ANISO module is found to be similar to the  $J_{\text{dip}}$  estimated using eq 1 (+0.019 vs +0.03). For the POLY\_ANISO simulation yield  $U_{\text{cal}} = 167$  K, though, in the ground state, there are states which have magnetic moments closer to zero magnetic moments (see Figure S46 in the SI), which is likely to offer a very strong QTM process. Although small ( $4 \times 10^{-7} \text{ cm}^{-1}$ ), the tunnel splitting computed is relatively high enough to offer tunneling in the ground state, as observed from experiments. This also rationalizes the relatively larger  $U_{\text{cal}}$  obtained from the calculations compared to the experiment as this estimate obtained from the *ab initio* relaxation mechanism did not factor in the tunneling process at the ground pseudo-doublet states.

The probable S-shape behavior of the  $M$  vs  $H$  curve, along with the arrangement of the single-ion calculated anisotropy axis, indicates the presence of the toroidal magnetic state in complex 2. The toroidal behavior for complex 2 has been investigated using the POLY\_ANISO module. The flipping of spin and hence the direction of anisotropic axis in the low-lying toroidal states are represented in Figure 16. The observed experimental  $U_{\text{eff}}$  value is much smaller than the POLY\_ANISO computed value for complex 2. This suggests that weak Dy...Dy coupling is likely to be overcome at the measured temperature leading to the observation of single-ion relaxation. A significant dipolar coupling (+0.02 to +0.045, see Table 4) in the Dy–Dy centers in complex 2 plays a dominating role in determining the toroidal magnetic state as

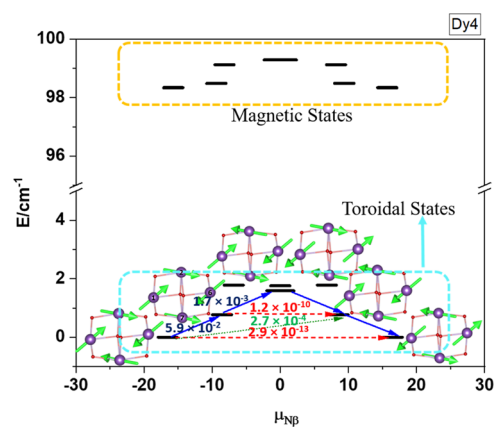


**Figure 16.** Poly\_ANISO-generated toroidal states for complex 2 (Dy<sub>4</sub>).

four Dy<sup>III</sup> centers form a circular arrangement of anisotropy. The local magnetization vector and major anisotropy axis are collinear due to the magnetic exchange, resulting in a noncompensated ground-state magnetic moment. As a result, the presence of a toroidal magnetic moment in complex 2 is categorized as a mixed-moment single-molecule toroid due to the dipolar ferromagnetic orientation of the pseudo-spins on Dy sites and the large magnetic moment of Dy sites in the ground exchange doublet (SMT). However, contrary to this, the arrangement of the anisotropy axis in complex 3 does not indicate any toroidal magnetic state. This is in accordance with the experimental field dependence of the magnetization curve, where no S-shape was detected. For complex 3, no toroidal arrangement was noted and the POLY\_ANISO fitting gives an energy barrier of  $29 \text{ cm}^{-1}$ , which is slightly less compared to the  $U_{\text{eff}}$  ( $43 \text{ cm}^{-1}$ , Figure S47).

## CONCLUSIONS

In summary, we have synthesized three dysprosium complexes with varying nuclearity {Dy<sub>2</sub>}, {Dy<sub>4</sub>}, and {Dy<sub>6</sub>} using a flexible arylohydrazone Schiff base ligand by changing the metal-to-ligand ratio and either the Dy<sup>III</sup> salt or the base (triethylamine to tetrabutylammonium) in combination with a coligand. Complex 1 is a dinuclear complex with nine coordinated metal centers and spherical tricapped trigonal prism coordination geometry, while 2 is a tetranuclear complex in a butterfly-shaped topology. 3 is a homometallic hexanuclear assembly where three atmospheric carbon dioxide molecules are trapped in the complex in the form of a carbonate ligand. DC magnetic measurements of 1–3 reveal that room-temperature  $\chi_M T$  values match well with expected values. AC susceptibility measurements of 1–3 reveal that all of the complexes show relaxation of magnetization in zero applied field. Temperature and field dependences of the relaxation times suggest that the magnetization relaxation in complex 1 takes place through a combination of QTM, Raman, and Orbach processes, while in complex 2, it occurs either through QTM and Orbach processes or via two Orbach processes. In the case of complex 3, the relaxation at zero field takes place through either a combination of Raman and Orbach processes or via two Orbach processes. Complex 1 under zero field has  $U_{\text{eff}}$  and  $\tau_0$  values of 87(1) K and  $\tau_0 = 6.4(3) \times 10^{-9}$  s. For complex 2,  $U_{\text{eff}} = 31(2)$  K,  $\tau_0 = 4.2(1) \times 10^{-7}$  s or  $\tau_{01} = 2(1) \times 10^{-7}$  s,  $U_{\text{eff}1} = 37(8)$  K,  $\tau_{02} = 5(6) \times 10^{-5}$  s,  $U_{\text{eff}2} = 8(4)$  by considering two Orbach relaxation processes. At zero-applied

magnetic field, **3** shows a double relaxation of magnetization characterized by  $\tau_{01} = 4(1) \times 10^{-8}$  s,  $U_{\text{eff}1} = 62.4(3)$  K,  $\tau_{02} = 4.6(2) \times 10^{-5}$  s,  $U_{\text{eff}2} = 2.1(2)$  K. *Ab initio* calculations suggest that due to the weak magnetic coupling between the metal centers, the magnetic relaxation is dominated by the single Dy<sup>III</sup> centers rather than the exchange-coupled state. Taking this into account, the dynamic properties of **1–3** can be rationalized on the basis of the shortest Dy–O bonds, their distribution on the Dy<sup>III</sup> coordination sphere, as well as the different types of Dy<sup>III</sup> ions present in the structure. Furthermore, for complex **2**, the toroidal magnetic state has been investigated and confirmed with the help of theoretical tools.

## ■ ASSOCIATED CONTENT

### SI Supporting Information

The Supporting Information is available free of charge at <https://pubs.acs.org/doi/10.1021/acs.inorgchem.2c01041>.

Simulated single-crystal data and experimental XRD pattern for **1–3**, continuous shape measurement calculations, supramolecular interactions of **1–3**, second derivative of  $\chi_M$  vs  $T$  plot, temperature dependence of  $\chi_M T$ , quantitative calculation of the anisotropic axis orientation using Chilton's method, temperature dependence of  $\chi_M T$  and Cole–Cole plot for **1** at zero and applied field, temperature dependence of  $\chi_M''$  at different frequencies, field dependence of relaxation times for **2** and **3**, frequency dependence of  $\chi_M''$  at different temperatures, normalized Cole–Cole plots for **2** and **3** under zero and an applied magnetic field, LoProp charge around the Dy centers, computed Loprop charge for complexes **1**, **2**, and **3**, and POLY\_ANISO computed low-lying energy spectrum of the exchanged coupled state for the complex Dy<sub>2</sub> (**1**) and Dy<sub>6</sub> (**3**) (PDF)

## ■ AUTHOR INFORMATION

### Corresponding Authors

**Gopalan Rajaraman** – Department of Chemistry, Indian Institute of Technology Bombay, Mumbai 400076, India; [orcid.org/0000-0001-6133-3026](https://orcid.org/0000-0001-6133-3026); Email: [rajaraman@chem.iitb.ac.in](mailto:rajaraman@chem.iitb.ac.in)

**Enrique Colacio** – Department of Inorganic Chemistry, University of Granada, 18071 Granada, Spain; Email: [ecolacio@ugr.es](mailto:ecolacio@ugr.es)

**Vadapalli Chandrasekhar** – Department of Chemistry, Indian Institute of Technology Kanpur, Kanpur 208016, India; Tata Institute of Fundamental Research Hyderabad, Hyderabad 500 107, India; [orcid.org/0000-0003-1968-2980](https://orcid.org/0000-0003-1968-2980); Email: [vc@iitk.ac.in](mailto:vc@iitk.ac.in), [vc@tifrh.res.in](mailto:vc@tifrh.res.in)

### Authors

**Pawan Kumar** – Department of Chemistry, Indian Institute of Technology Kanpur, Kanpur 208016, India

**Abinash Swain** – Department of Chemistry, Indian Institute of Technology Bombay, Mumbai 400076, India

**Joydev Acharya** – Department of Chemistry, Indian Institute of Technology Kanpur, Kanpur 208016, India

**Yanling Li** – Sorbonne Universit Institut Parisien de Chimie Molculaire, CNRS UMR 8232, 75252 Paris cedex 5, France

**Vierandra Kumar** – Department of Chemistry, Indian Institute of Technology Kanpur, Kanpur 208016, India

Complete contact information is available at:

<https://pubs.acs.org/10.1021/acs.inorgchem.2c01041>

## Notes

The authors declare no competing financial interest.

## ■ ACKNOWLEDGMENTS

The authors thank the Department of Science and Technology (DST), India, and support from the Single Crystal CCD X-ray Diffractometer facility at IIT-Kanpur. V.C. is grateful to the DST for a J. C. Bose fellowship. P.K. and A.S. thank University Grants Commission (UGC), India, for Senior Research Fellowship. G.R. acknowledges DST/SERB for funding (CRG/2018/000430; DST/SJF/CSA-03/2018-10; SB/SJF/2019-20/12). Financial support from the Spanish Ministerio de Ciencia e Innovación project (PGC2018 102052-B-C21) MCIN/AEI/10.13039/501100011033/FEDER “Una manera de hacer Europa”, to Junta de Andalucía (FQM-195) and the projects I+D+i Junta de Andalucía (P20\_00692) and FEDER Junta de Andalucía (A-FQM-172-UGR18) and the University of Granada are also acknowledged.

## ■ REFERENCES

- (1) Ishikawa, N.; Sugita, M.; Ishikawa, T.; Koshihara, S.-y.; Kaizu, Y. Lanthanide Double-Decker Complexes Functioning as Magnets at the Single-Molecule Level. *J. Am. Chem. Soc.* **2003**, *125*, 8694–8695.
- (2) (a) Sessoli, R.; Powell, A. K. Strategies towards single molecule magnets based on lanthanide ions. *Coord. Chem. Rev.* **2009**, *253*, 2328–2341. (b) Woodruff, D. N.; Winpenny, R. E. P.; Layfield, R. A. Lanthanide Single-Molecule Magnets. *Chem. Rev.* **2013**, *113*, 5110–5148. (c) Dey, A.; Kalita, P.; Chandrasekhar, V. Lanthanide(III)-Based Single-Ion Magnets. *ACS Omega* **2018**, *3*, 9462–9475. (d) Zhu, Z.; Guo, M.; Li, X.-L.; Tang, J. Molecular magnetism of lanthanide: Advances and perspectives. *Coord. Chem. Rev.* **2019**, *378*, 350–364. (e) Goodwin, C. A. P. Blocking like it's hot: a synthetic chemists' path to high-temperature lanthanide single molecule magnets. *Dalton Trans.* **2020**, *49*, 14320–14337.
- (3) (a) Feltham, H. L. C.; Brooker, S. Review of purely 4f and mixed-metal nd-4f single-molecule magnets containing only one lanthanide ion. *Coord. Chem. Rev.* **2014**, *276*, 1–33. (b) Liu, J.-L.; Chen, Y.-C.; Tong, M.-L. Symmetry strategies for high performance lanthanide-based single-molecule magnets. *Chem. Soc. Rev.* **2018**, *47*, 2431–2453. (c) Acharya, J.; Kalita, P.; Chandrasekhar, V. High-Coordinate Mononuclear Ln(III) Complexes: Synthetic Strategies and Magnetic Properties. *Magnetochemistry* **2021**, *7*, 1. (d) Zabala-Lekuona, A.; Seco, J. M.; Colacio, E. Single-Molecule Magnets: From Mn12-ac to dysprosium metallocenes, a travel in time. *Coord. Chem. Rev.* **2021**, *441*, No. 213984. (e) Parmar, V. S.; Mills, D. P.; Winpenny, R. E. P. Mononuclear Dysprosium Alkoxide and Aryloxide Single-Molecule Magnets. *Chem. – Eur. J.* **2021**, *27*, 7625–7645.
- (4) (a) Goodwin, C. A. P.; Ortu, F.; Reta, D.; Chilton, N. F.; Mills, D. P. Molecular magnetic hysteresis at 60 kelvin in dysprosocenium. *Nature* **2017**, *548*, 439–442. (b) Guo, F.-S.; Day, B. M.; Chen, Y.-C.; Tong, M.-L.; Mansikkamäki, A.; Layfield, R. A. Magnetic hysteresis up to 80 kelvin in a dysprosium metallocene single-molecule magnet. *Science* **2018**, *362*, 1400.
- (5) (a) Chen, Y.-C.; Liu, J.-L.; Ungur, L.; Liu, J.; Li, Q.-W.; Wang, L.-F.; Ni, Z.-P.; Chibotaru, L. F.; Chen, X.-M.; Tong, M.-L. Symmetry-Supported Magnetic Blocking at 20 K in Pentagonal Bipyramidal Dy(III) Single-Ion Magnets. *J. Am. Chem. Soc.* **2016**, *138*, 2829–2837. (b) Liu, J.; Chen, Y.-C.; Liu, J.-L.; Vieru, V.; Ungur, L.; Jia, J.-H.; Chibotaru, L. F.; Lan, Y.; Wernsdorfer, W.; Gao, S.; Chen, X.-M.; Tong, M.-L. A Stable Pentagonal Bipyramidal Dy(III) Single-Ion Magnet with a Record Magnetization Reversal Barrier over 1000 K. *J. Am. Chem. Soc.* **2016**, *138*, 5441–5450. (c) Gupta, S. K.; Rajeshkumar, T.; Rajaraman, G.; Murugavel, R. An air-stable Dy(III) single-ion magnet with high anisotropy barrier and blocking temperature. *Chem. Sci.* **2016**, *7*, 5181–5191. (d) Ding, Y.-S.;

- Chilton, N. F.; Winpenny, R. E. P.; Zheng, Y.-Z. On Approaching the Limit of Molecular Magnetic Anisotropy: A Near-Perfect Pentagonal Bipyramidal Dysprosium(III) Single-Molecule Magnet. *Angew. Chem., Int. Ed.* **2016**, *55*, 16071–16074. (e) Jiang, Z.; Sun, L.; Yang, Q.; Yin, B.; Ke, H.; Han, J.; Wei, Q.; Xie, G.; Chen, S. Excess axial electrostatic repulsion as a criterion for pentagonal bipyramidal Dy<sup>III</sup> single-ion magnets with high Ueff and TB. *J. Mater. Chem. C* **2018**, *6*, 4273–4280.
- (6) (a) Biswas, S.; Bejoymohandas, K. S.; Das, S.; Kalita, P.; Reddy, M. L. P.; Oyarzabal, I.; Colacio, E.; Chandrasekhar, V. Mononuclear Lanthanide Complexes: Energy-Barrier Enhancement by Ligand Substitution in Field-Induced Dy(III) SIMs. *Inorg. Chem.* **2017**, *56*, 7985–7997. (b) Bar, A. K.; Kalita, P.; Sutter, J.-P.; Chandrasekhar, V. Pentagonal-Bipyramid Ln(III) Complexes Exhibiting Single-Ion-Magnet Behavior: A Rational Synthetic Approach for a Rigid Equatorial Plane. *Inorg. Chem.* **2018**, *57*, 2398–2401. (c) Kalita, P.; Malakar, A.; Goura, J.; Nayak, S.; Herrera, J. M.; Colacio, E.; Chandrasekhar, V. Mononuclear lanthanide complexes assembled from a tridentate NNO donor ligand: design of a Dy (III) single-ion magnet. *Dalton Trans.* **2019**, *48*, 4857–4866. (d) Kalita, P.; Ahmed, N.; Bar, A. K.; Dey, S.; Jana, A.; Rajaraman, G.; Sutter, J.-P.; Chandrasekhar, V. Pentagonal Bipyramidal Ln(III) Complexes Containing an Axial Phosphine Oxide Ligand: Field-induced Single-ion Magnetism Behavior of the Dy(III) Analogues. *Inorg. Chem.* **2020**, *59*, 6603–6612. (e) Kalita, P.; Nayak, P.; Ahmed, N.; Herrera, J. M.; Venkatasubbiah, K.; Colacio, E.; Chandrasekhar, V. Seven-coordinate Ln (III) complexes assembled from a bulky MesacacH ligand: their synthesis, structure, photoluminescence and SMM behaviour. *Dalton Trans.* **2020**, *49*, 15404–15416. (f) Diaz-Ortega, I. F.; Herrera, J. M.; Dey, S.; Nojiri, H.; Rajaraman, G.; Colacio, E. The effect of the electronic structure and flexibility of the counteranions on magnetization relaxation in [Dy(L)<sub>2</sub>(H<sub>2</sub>O)<sub>3</sub>]<sup>3+</sup> (L = phosphine oxide derivative) pentagonal bipyramidal SIMs. *Inorg. Chem. Front.* **2020**, *7*, 689–699.
- (7) (a) Guo, Y.-N.; Xu, G.-F.; Wernsdorfer, W.; Ungur, L.; Guo, Y.; Tang, J.; Zhang, H.-J.; Chibotaru, L. F.; Powell, A. K. Strong Axiality and Ising Exchange Interaction Suppress Zero-Field Tunneling of Magnetization of an Asymmetric Dy<sub>2</sub> Single-Molecule Magnet. *J. Am. Chem. Soc.* **2011**, *133*, 11948–11951. (b) Long, J.; Habib, F.; Lin, P.-H.; Korobkov, I.; Enright, G.; Ungur, L.; Wernsdorfer, W.; Chibotaru, L. F.; Murugesu, M. Single-Molecule Magnet Behavior for an Antiferromagnetically Superexchange-Coupled Dinuclear Dysprosium(III) Complex. *J. Am. Chem. Soc.* **2011**, *133*, 5319–5328. (c) Rinehart, J. D.; Fang, M.; Evans, W. J.; Long, J. R. A N23–Radical-Bridged Terbium Complex Exhibiting Magnetic Hysteresis at 14 K. *J. Am. Chem. Soc.* **2011**, *133*, 14236–14239. (d) Moreno Pineda, E.; Chilton, N. F.; Marx, R.; Dörfel, M.; Sells, D. O.; Neugebauer, P.; Jiang, S.-D.; Collison, D.; van Slageren, J.; McInnes, E. J. L.; Winpenny, R. E. P. Direct measurement of dysprosium-(III)dysprosium(III) interactions in a single-molecule magnet. *Nat. Commun.* **2014**, *5*, No. 5243. (e) Rinehart, J. D.; Fang, M.; Evans, W. J.; Long, J. R. Strong exchange and magnetic blocking in N23–radical-bridged lanthanide complexes. *Nature Chem.* **2011**, *3*, 538–542. (f) Guo, F.-S.; Layfield, R. A. Strong direct exchange coupling and single-molecule magnetism in indigo-bridged lanthanide dimers. *Chem. Commun.* **2017**, *53*, 3130–3133. (g) Zhang, L.; Zhang, Y.-Q.; Zhang, P.; Zhao, L.; Guo, M.; Tang, J. Single-Molecule Magnet Behavior Enhanced by Synergic Effect of Single-Ion Anisotropy and Magnetic Interactions. *Inorg. Chem.* **2017**, *56*, 7882–7889. (h) Han, T.; Ding, Y.-S.; Li, Z.-H.; Yu, K.-X.; Zhai, Y.-Q.; Chilton, N. F.; Zheng, Y.-Z. A dichlorido-bridged dinuclear Dy(III) single-molecule magnet with an effective energy barrier larger than 600 K. *Chem. Commun.* **2019**, *55*, 7930–7933. (i) Acharya, J.; Ahmed, N.; Flores Gonzalez, J.; Kumar, P.; Cador, O.; Singh, S. K.; Pointillart, F.; Chandrasekhar, V. Slow magnetic relaxation in a homo dinuclear Dy(III) complex in a pentagonal bipyramidal geometry. *Dalton Trans.* **2020**, *49*, 13110–13122.
- (8) (a) Evangelisti, M.; Brechin, E. K. Recipes for enhanced molecular cooling. *Dalton Trans.* **2010**, *39*, 4672–4676. (b) Lorusso, G.; Palacios, M. A.; Nichol, G. S.; Brechin, E. K.; Roubeau, O.; Evangelisti, M. Increasing the dimensionality of cryogenic molecular coolers: Gd-based polymers and metal–organic frameworks. *Chem. Commun.* **2012**, *48*, 7592–7594. (c) Sessoli, R. Chilling with Magnetic Molecules. *Angew. Chem., Int. Ed.* **2012**, *51*, 43–45. (d) Liu, J.-L.; Chen, Y.-C.; Guo, F.-S.; Tong, M.-L. Recent advances in the design of magnetic molecules for use as cryogenic magnetic coolants. *Coord. Chem. Rev.* **2014**, *281*, 26–49. (e) Luo, X.-M.; Hu, Z.-B.; Lin, Q.-f.; Cheng, W.; Cao, J.-P.; Cui, C.-H.; Mei, H.; Song, Y.; Xu, Y. Exploring the Performance Improvement of Magnetocaloric Effect Based Gd-Exclusive Cluster Gd<sub>60</sub>. *J. Am. Chem. Soc.* **2018**, *140*, 11219–11222. (f) Liu, S.-J.; Han, S.-D.; Zhao, J.-P.; Xu, J.; Bu, X.-H. In-situ synthesis of molecular magnetorefrigerant materials. *Coord. Chem. Rev.* **2019**, *394*, 39–52.
- (9) (a) Ungur, L.; Lin, S.-Y.; Tang, J.; Chibotaru, L. F. Single-molecule toroics in Ising-type lanthanide molecular clusters. *Chem. Soc. Rev.* **2014**, *43*, 6894–6905. (b) Li, X.-L.; Tang, J. Recent developments in single-molecule toroics. *Dalton Trans.* **2019**, *48*, 15358–15370. (c) Vignesh, K. R.; Rajaraman, G. Strategies to Design Single-Molecule Toroics Using Triangular {Ln<sub>3</sub>}<sub>n</sub> Motifs. *ACS Omega* **2021**, *6*, 32349–32364.
- (10) (a) Das, S.; Hossain, S.; Dey, A.; Biswas, S.; Sutter, J.-P.; Chandrasekhar, V. Molecular Magnets Based on Homometallic Hexanuclear Lanthanide(III) Complexes. *Inorg. Chem.* **2014**, *53*, 5020–5028. (b) Biswas, S.; Das, S.; Gupta, T.; Singh, S. K.; Pissas, M.; Rajaraman, G.; Chandrasekhar, V. Observation of Slow Relaxation and Single-Molecule Toroidal Behavior in a Family of Butterfly-Shaped Ln<sub>4</sub> Complexes. *Chem. – Eur. J.* **2016**, *22*, 18532–18550. (c) Biswas, S.; Das, S.; Acharya, J.; Kumar, V.; van Leusen, J.; Kögerler, P.; Herrera, J. M.; Colacio, E.; Chandrasekhar, V. Homometallic Dy (III) Complexes of Varying Nuclearity from 2 to 21: Synthesis, Structure, and Magnetism. *Chem. – Eur. J.* **2017**, *23*, 5154–5170. (d) Biswas, S.; Kumar, P.; Swain, A.; Gupta, T.; Kalita, P.; Kundu, S.; Rajaraman, G.; Chandrasekhar, V. Phosphonate-assisted tetranuclear lanthanide assemblies: observation of the toroidal ground state in the Tb (III) analogue. *Dalton Trans.* **2019**, *48*, 6421–6434. (e) Kumar, P.; Biswas, S.; Swain, A.; Acharya, J.; Kumar, V.; Kalita, P.; Gonzalez, J. F.; Cador, O.; Pointillart, F.; Rajaraman, G.; Chandrasekhar, V. Azide-Coordination in Homometallic Dinuclear Lanthanide (III) Complexes Containing Nonequivalent Lanthanide Metal Ions: Zero-Field SMM Behavior in the Dysprosium Analogue. *Inorg. Chem.* **2021**, *60*, 8530–8545.
- (11) (a) Vogel, A. I.; Furniss, B. S.; Hannaford, A. J.; Smith, P. W. G.; Tatchell, A. R. *Vogel's Textbook of Practical Organic Chemistry*, 5th ed.; Longman: Harlow, 1989. (b) Williams, D. B. G.; Lawton, M. Drying of Organic Solvents: Quantitative Evaluation of the Efficiency of Several Desiccants. *J. Org. Chem.* **2010**, *75*, 8351–8354.
- (12) (a) SMART; SAINT, Software Reference manuals, version 6.45. 2003. (b) Sheldrick, G. SADABS, *Software for Empirical Absorption Correction*, ver. 2.05; University of Göttingen: Göttingen, Germany, 2002. (c) SHELXTL Reference Manual; Bruker Analytical X-ray Systems, Inc.: Madison, WI, 2000. (d) *CrysAlis PRO*, Rigaku Oxford Diffraction: Yarnton, England, 2015. (e) Sheldrick, G. M. A short history of SHELX. *Acta Crystallogr., Sect. A: Found. Crystallogr.* **2008**, *64*, 112–122. (f) Dolomanov, O. V.; Bourhis, L. J.; Gildea, R. J.; Howard, J. A. K.; Puschmann, H. OLEX2: a complete structure solution, refinement and analysis program. *J. Appl. Crystallogr.* **2009**, *42*, 339–341. (g) Bradenburg, K. *Diamond*, version 3.1 e; Crystal Impact GbR: Bonn, Germany, 2005.
- (13) (a) Fdez Galván, I.; Vacher, M.; Alavi, A.; Angeli, C.; Aquilante, R.; Autschbach, J.; Bao, J. J.; Bokarev, S. I.; Bogdanov, N. A.; Carlson, F. K.; Chibotaru, L. F.; Creutzberg, J.; Dattani, N.; Delcey, M. G.; Dong, S. S.; Dreuw, A.; Freitag, L.; Frutos, L. M.; Gagliardi, L.; Gendron, F.; Giussani, A.; González, L.; Grell, G.; Guo, M.; Hoyer, C. E.; Johansson, M.; Keller, S.; Knecht, S.; Kovačević, G.; Källman, E.; Li Manni, G.; Lundberg, M.; Ma, Y.; Mai, S.; Malhado, J. P.; Malmqvist, PÅ.; Marquetand, P.; Mewes, S. A.; Norell, J.; Olivucci, M.; Oppel, M.; Phung, Q. M.; Pierloot, K.; Plasser, F.; Reiher, M.; Sand, A. M.; Schapiro, I.; Sharma, P.; Stein, C. J.; Sorensen, L. K.;

- Truhlar, D. G.; Ugandi, M.; Ungur, L.; Valentini, A.; Vancoillie, S.; Verezov, V.; Weser, O.; Wesolowski, T. A.; Widmark, P.-O.; Wouters, S.; Zech, A.; Zobel, J. P.; Lindh, R. OpenMolcas: From Source Code to Insight. *J. Chem. Theory Comput.* **2019**, *15*, 5925–5964. (b) Swerts, B.; Chibotaru, L. F.; Lindh, R.; Seijo, L.; Barandiaran, Z.; Clima, S.; Pierloot, K.; Hendrickx, M. F. A. Embedding Fragment ab Initio Model Potentials in CASSCF/CASPT2 Calculations of Doped Solids. *J. Chem. Theory Comput.* **2008**, *4*, 586–594. (c) Malmqvist, P. Å.; Roos, B. O.; Schimmelpfennig, B. The restricted active space (RAS) state interaction approach with spin–orbit coupling. *Chem. Phys. Lett.* **2002**, *357*, 230–240. (d) Chibotaru, L. F.; Ceulemans, A.; Bolvin, H. Unique Definition of the Zeeman-Splitting  $g$  Tensor of a Kramers Doublet. *Phys. Rev. Lett.* **2008**, *101*, No. 033003. (e) Chibotaru, L. F.; Ungur, L. Ab initio calculation of anisotropic magnetic properties of complexes. I. Unique definition of pseudospin Hamiltonians and their derivation. *J. Chem. Phys.* **2012**, *137*, No. 064112. (f) Chibotaru, L. F.; Ungur, L. University of Leuven, 2006, <https://chem.kuleuven.be/en/research/qcpc/ton/software-1>. (g) Chibotaru, L.; Ungur, L.; Ungur, L. F. Chibotaru in <http://www.molcas.org/documentation/manual/node105.html>. (h) Roos, B. O.; Lindh, R.; Malmqvist, P.-Å.; Verezov, V.; Widmark, P.-O. Main Group Atoms and Dimers Studied with a New Relativistic ANO Basis Set. *J. Phys. Chem. A* **2004**, *108*, 2851–2858. (i) Zobel, J. P.; Widmark, P.-O.; Verezov, V. The ANO-R Basis Set. *J. Chem. Theory Comput.* **2020**, *16*, 278–294. (j) Nakajima, T.; Hirao, K. The Douglas–Kroll–Hess Approach. *Chem. Rev.* **2012**, *112*, 385–402. (k) Vignesh, K. R.; Langley, S. K.; Murray, K. S.; Rajaraman, G. Exploring the Influence of Diamagnetic Ions on the Mechanism of Magnetization Relaxation in  $\{\text{Co}(\text{III})_2\text{Ln}(\text{III})_2\}$  (Ln = Dy, Tb, Ho) “Butterfly” Complexes. *Inorg. Chem.* **2017**, *56*, 2518–2532. (l) Risch, M.; Trucks, G.; Schlegel, H.; Scuseria, G.; Robb, M.; Cheeseman, J.; Scalmani, G.; Barone, V.; Petersson, G.; Nakatsuji, H. Gaussian, Inc.: Wallingford CT, 2016, <https://gaussian.com/citation/>. (m) Becke, A. D. Density-functional thermochemistry. III. The role of exact exchange. *J. Chem. Phys.* **1993**, *98*, 5648–5652. (n) Cundari, T. R.; Stevens, W. J. Effective core potential methods for the lanthanides. *J. Chem. Phys.* **1993**, *98*, 5555–5565. (o) Schäfer, A.; Huber, C.; Ahlrichs, R. Fully optimized contracted Gaussian basis sets of triple zeta valence quality for atoms Li to Kr. *J. Chem. Phys.* **1994**, *100*, 5829–5835. (p) Chibotaru, L. F.; F, L.; Ungur, L. *Program POLY\_ANISO*; KU Leuven: Leuven, Belgium, 2007.
- (14) (a) Soltys-Brzostek, K.; Terlecki, M.; Sokolowski, K.; Lewiński, J. Chemical fixation and conversion of CO<sub>2</sub> into cyclic and cage-type metal carbonates. *Coord. Chem. Rev.* **2017**, *334*, 199–231. (b) Mateus, P.; Delgado, R.; Lloret, F.; Cano, J.; Brandão, P.; Félix, V. A Trinuclear Copper(II) Cryptate and Its  $\mu_3$ -CO<sub>3</sub> Cascade Complex: Thermodynamics, Structural and Magnetic Properties. *Chem. – Eur. J.* **2011**, *17*, 11193–11203. (c) Anderson, J. C.; Blake, A. J.; Moreno, R. B.; Raynel, G.; van Slageren, J. A novel tridentate coordination mode for the carbonatonickel system exhibited in an unusual hexanuclear nickel(ii)  $\mu_3$ -carbonato-bridged complex. *Dalton Trans.* **2009**, 9153–9156. (d) Ghosh, A. K.; Pait, M.; Shatruck, M.; Bertolasi, V.; Ray, D. Self-assembly of a [Ni<sub>8</sub>] carbonate cube incorporating four  $\mu_4$ -carbonato linkers through fixation of atmospheric CO<sub>2</sub> by ligated [Ni<sub>2</sub>] complexes. *Dalton Trans.* **2014**, *43*, 1970–1973. (e) Titos-Padilla, S.; Ruiz, J.; Herrera, J. M.; Brechin, E. K.; Wersndorfer, W.; Lloret, F.; Colacio, E. Dilution-Triggered SMM Behavior under Zero Field in a Luminescent Zn<sub>2</sub>Dy<sub>2</sub> Tetranuclear Complex Incorporating Carbonato-Bridging Ligands Derived from Atmospheric CO<sub>2</sub> Fixation. *Inorg. Chem.* **2013**, *52*, 9620–9626. (f) Goura, J.; Colacio, E.; Herrera, J. M.; Suturina, E. A.; Kuprov, I.; Lan, Y.; Wersndorfer, W.; Chandrasekhar, V. Heterometallic Zn<sub>3</sub>Ln<sub>3</sub> Ensembles Containing ( $\mu_6$ -CO<sub>3</sub>) Ligand and Triangular Disposition of Ln<sup>3+</sup> ions: Analysis of Single-Molecule Toroid (SMT) and Single-Molecule Magnet (SMM) Behavior. *Chem. – Eur. J.* **2017**, *23*, 16621–16636. (g) Pasatoiu, T. D.; Ghiurri, A.; Madalan, A. M.; Affronte, M.; Andruh, M. Octanuclear [Ni(II)<sub>4</sub>Ln(III)<sub>4</sub>] complexes. Synthesis, crystal structures and magnetocaloric properties. *Dalton Trans.* **2014**, *43*, 9136–9142. (h) Langley, S. K.; Moubaraki, B.; Murray, K. S. Magnetic Properties of Hexanuclear Lanthanide(III) Clusters Incorporating a Central  $\mu_6$ -Carbonate Ligand Derived from Atmospheric CO<sub>2</sub> Fixation. *Inorg. Chem.* **2012**, *51*, 3947–3949. (i) Andrews, P. C.; Beck, T.; Forsyth, C. M.; Fraser, B. H.; Junk, P. C.; Massi, M.; Roesky, P. W. Templated assembly of a  $\mu_6$ -CO<sub>3</sub><sup>2-</sup> dodecanuclear lanthanum dibenzoylmethanide hydroxido cluster with concomitant formation of phenylglyoxylate. *Dalton Trans.* **2007**, 5651–5654. (j) Holmberg, R. J.; Kuo, C.-J.; Gabidullin, B.; Wang, C.-W.; Clérac, R.; Murugesu, M.; Lin, P.-H. A propeller-shaped  $\mu_4$ -carbonate hexanuclear dysprosium complex with a high energetic barrier to magnetisation relaxation. *Dalton Trans.* **2016**, *45*, 16769–16773. (k) Hołyńska, M.; Clérac, R.; Rouzières, M. Lanthanide Complexes with Multidentate Oxime Ligands as Single-Molecule Magnets and Atmospheric Carbon Dioxide Fixation Systems. *Chem. – Eur. J.* **2015**, *21*, 13321–13329. (l) Tian, H.; Zhao, L.; Tang, J. Exploiting Miraculous Atmospheric CO<sub>2</sub> Fixation in the Design of Dysprosium Single-Molecule Magnets. *Cryst. Growth Des.* **2018**, *18*, 1173–1181. (m) Wang, W.-M.; Wu, Z.-L.; Zhang, Y.-X.; Wei, H.-Y.; Gao, H.-L.; Cui, J.-Z. Self-assembly of tetra-nuclear lanthanide clusters via atmospheric CO<sub>2</sub> fixation: interesting solvent-induced structures and magnetic relaxation conversions. *Inorg. Chem. Front.* **2018**, *5*, 2346–2354.
- (15) (a) Cirera, J.; Ruiz, E.; Alvarez, S. Continuous Shape Measures as a Stereochemical Tool in Organometallic Chemistry. *Organometallics* **2005**, *24*, 1556–1562. (b) *SHAPE: Continuous Shape Measures Calculation 2.1; Electronic Structure Group*, Universitat de Barcelona: Spain, 2013.
- (16) (a) Kalita, P.; Goura, J.; Manuel Herrera Martínez, J.; Colacio, E.; Chandrasekhar, V. Homodinuclear {Ln(III)<sub>2</sub>} (Ln(III) = Gd(III), Tb(III), Ho(III), and Dy(III)) Complexes: Field-Induced SMM Behavior of the Dy(III) and Tb(III) Analogues. *Eur. J. Inorg. Chem.* **2019**, *2019*, 212–220. (b) Bi, Y.; Guo, Y.-N.; Zhao, L.; Guo, Y.; Lin, S.-Y.; Jiang, S.-D.; Tang, J.; Wang, B.-W.; Gao, S. Capping Ligand Perturbed Slow Magnetic Relaxation in Dysprosium Single-Ion Magnets. *Chem. – Eur. J.* **2011**, *17*, 12476–12481. (c) Feltham, H. L. C.; Lan, Y.; Klöwer, F.; Ungur, L.; Chibotaru, L. F.; Powell, A. K.; Brooker, S. A Non-sandwiched Macrocyclic Monolanthanide Single-Molecule Magnet: The Key Role of Axiality. *Chem. – Eur. J.* **2011**, *17*, 4362–4365.
- (17) (a) Hänninen, M. M.; Mota, A. J.; Aravena, D.; Ruiz, E.; Sillanpää, R.; Camón, A.; Evangelisti, M.; Colacio, E. Two C<sub>3</sub>-Symmetric Dy<sub>3</sub>(III) Complexes with Triple Di- $\mu$ -methoxy- $\mu$ -phenoxo Bridges, Magnetic Ground State, and Single-Molecule Magnetic Behavior. *Chem. – Eur. J.* **2014**, *20*, 8410–8420. (b) Pointillart, F.; Golhen, S.; Cadot, O.; Ouahab, L. Slow Magnetic Relaxation in a Redox-Active Tetraiafulvalene-Based Ferromagnetic Dysprosium Complex. *Eur. J. Inorg. Chem.* **2014**, *2014*, 4558–4563.
- (18) Chilton, N. F.; Collison, D.; McInnes, E. J. L.; Winpenny, R. E. P.; Soncini, A. An electrostatic model for the determination of magnetic anisotropy in dysprosium complexes. *Nat. Commun.* **2013**, *4*, No. 2551.
- (19) (a) Guo, Y.-N.; Chen, X.-H.; Xue, S.; Tang, J. Modulating Magnetic Dynamics of Three Dy<sub>2</sub> Complexes through Keto–Enol Tautomerism of the o-Vanillin Picolinoylhydrazone Ligand. *Inorg. Chem.* **2011**, *50*, 9705–9713. (b) Zou, L.; Zhao, L.; Chen, P.; Guo, Y.-N.; Guo, Y.; Li, Y.-H.; Tang, J. Phenoxido and alkoxido-bridged dinuclear dysprosium complexes showing single-molecule magnet behaviour. *Dalton Trans.* **2012**, *41*, 2966–2971. (c) Maniaki, D.; Perlepe, P. S.; Pilichos, E.; Christodoulou, S.; Rouzières, M.; Dechambenoit, P.; Clérac, R.; Perlepes, S. P. Asymmetric Dinuclear Lanthanide(III) Complexes from the Use of a Ligand Derived from 2-Acetylpyridine and Picolinoylhydrazone: Synthetic, Structural and Magnetic Studies. *Molecules* **2020**, *25*, 3153.
- (20) Sutradhar, M.; Alegria, E. C. B. A.; Barman, T. R.; Guedes da Silva, M. F. C.; Liu, C.-M.; Pombeiro, A. J. L. 1D Copper(II)-Aroylhydrazone Coordination Polymers: Magnetic Properties and Microwave Assisted Oxidation of a Secondary Alcohol. *Front. Chem.* **2020**, *8*, 157.
- (21) (a) Ding, Y.-S.; Yu, K.-X.; Reta, D.; Ortu, F.; Winpenny, R. E. P.; Zheng, Y.-Z.; Chilton, N. F. Field- and temperature-dependent

quantum tunnelling of the magnetisation in a large barrier single-molecule magnet. *Nat. Commun.* **2018**, *9*, No. 3134. (b) Lucaccini, E.; Sorace, L.; Perfetti, M.; Costes, J.-P.; Sessoli, R. Beyond the anisotropy barrier: slow relaxation of the magnetization in both easy-axis and easy-plane Ln(trensal) complexes. *Chem. Commun.* **2014**, *50*, 1648–1651. (c) Galangau, O.; Flores Gonzalez, J.; Montigaud, V.; Dorcet, V.; le Guennic, B.; Cador, O.; Pointillart, F. Dysprosium Single-Molecule Magnets Involving 1,10-Phenantroline-5,6-dione Ligand. *Magnetochemistry* **2020**, *6*, 19.

(22) (a) Ishikawa, N.; Sugita, M.; Wernsdorfer, W. Quantum tunneling of magnetization in lanthanide single-molecule magnets: bis(phthalocyaninato) terbium and bis(phthalocyaninato)dysprosium anions. *Angew. Chem., Int. Ed.* **2005**, *44*, 2931–2935. (b) Pointillart, F.; Bernot, K.; Golhen, S.; LeGuennic, B.; Guizouarn, T.; Ouhab, L.; Cador, O. Magnetic memory in an isotopically enriched and magnetically isolated mononuclear dysprosium complex. *Angew. Chem., Int. Ed.* **2015**, *54*, 1504–1507. (c) Moreno-Pineda, E.; Damjanović, M.; Fuhr, O.; Wernsdorfer, W.; Ruben, M. Nuclear spin isomers: engineering a  $\text{Et}_4\text{N}[\text{DyPc}_2]$  spin qubit. *Angew. Chem., Int. Ed.* **2017**, *56*, 9915–9919. (d) Kishi, Y.; Pointillart, F.; Lefeuvre, B.; Riobé, F.; Le Guennic, B.; Golhen, S.; Cador, O.; Maury, O.; Fujiwara, H.; Ouahab, L. Isotopically enriched polymorphs of dysprosium single molecule magnets. *Chem. Commun.* **2017**, *53*, 3575–3578.

(23) Shrivastava, K. N. Theory of Spin–Lattice Relaxation. *Phys. Status Solidi B* **1983**, *117*, 437–458.

(24) (a) Ruiz, J.; Mota, A. J.; Rodríguez-Diéguez, A.; Titos, S.; Herrera, J. M.; Ruiz, E.; Cremades, E.; Costes, J. P.; Colacio, E. Field and dilution effects on the slow relaxation of a luminescent  $\text{DyO}_9$  low-symmetry single-ion magnet. *Chem. Commun.* **2012**, *48*, 7916–7918. (b) Das, S.; Dey, A.; Biswas, S.; Colacio, E.; Chandrasekhar, V. Hydroxide-Free Cubane-Shaped Tetranuclear  $[\text{Ln}_4]$  Complexes. *Inorg. Chem.* **2014**, *53*, 3417–3426. (c) Reis, S. G.; Briganti, M.; Soriano, S.; Guedes, G. P.; Calancea, S.; Tiseanu, C.; Novak, M. A.; del Águila Sanchez, M. A.; Totti, F.; Lopez-Ortiz, F.; Andruh, M.; Vaz, M. G. F.  $\nu$ . Binuclear lanthanide-radical complexes featuring two centers with different magnetic and luminescence properties. *Inorg. Chem.* **2016**, *55*, 11676–11684. (d) Díaz-Ortega, I.; Herrera, J. M.; Aravena, D.; Ruiz, E.; Gupta, T.; Rajaraman, G.; Nojiri, H.; Colacio, E. *Inorg. Chem.* **2018**, *57*, 6362–6375. (e) Andrea Mattei, C. A.; Lefeuvre, B.; Dorcet, V.; Argouarch, G.; Cador, O.; Lalli, C.; Pointillart, F. Counterintuitive Single-Molecule Magnet Behaviour in Two Polymorphs of One-Dimensional Compounds Involving Chiral BINOL-Derived Bisphosphate Ligands. *Magnetochemistry* **2021**, *7*, 150.

(25) Chilton, N. M. *CCFIT Program*; The Chilton Group: Manchester, U.K., 2014.

(26) Hu, L.; Reid, M. F.; Duan, C.-K.; Xia, S.; Yin, M. Extraction of crystal-field parameters for lanthanide ions from quantum-chemical calculations. *J. Phys.: Condens. Matter* **2011**, *23*, No. 045501.

(27) Dai, D.; Whangbo, M.-H. Spin exchange interactions of a spin dimer: Analysis of broken-symmetry spin states in terms of the eigenstates of Heisenberg and Ising spin Hamiltonians. *J. Chem. Phys.* **2003**, *118*, 29–39.

## Recommended by ACS

### Equatorially Positioned Halogen Ligand Effects on Single-Molecule Magnetism in a Mononuclear Dy(III) Octahedral Structure

Haipeng Wu, Sanping Chen, *et al.*

DECEMBER 01, 2022  
CRYSTAL GROWTH & DESIGN

READ 

### Assembly Studies of Two Planar Dy<sub>4</sub> Single-Molecule Magnets

Shui Yu, Zilu Chen, *et al.*

NOVEMBER 23, 2022  
CRYSTAL GROWTH & DESIGN

READ 

### Heteroleptic Dysprosium(III) Single-Molecule Magnets with Amidinate and Cyclopentadienyl Ligands

Yidian Wang, Yan-Zhen Zheng, *et al.*

OCTOBER 03, 2022  
CRYSTAL GROWTH & DESIGN

READ 

### Theoretical and Experimental Studies of the Magnetostructural Correlations in Mononuclear Dy<sup>III</sup> Compounds Evidenced by Quantum Tunneling of Magnet...

Sheng Zhang, Bing Yin, *et al.*

AUGUST 04, 2022  
CRYSTAL GROWTH & DESIGN

READ 

Get More Suggestions >